

Final Report

Project Title: High Temperature Falling Particle Receiver (2012 – 2016)

Project Period: 10/01/12 – 3/31/16

Budget Period: 10/01/12 – 3/31/16

Budget Period Budget: \$4,501,610

Submission Date: 4/15/2016

Recipient: Sandia National Laboratories

Address: P.O. Box 5800, MS-1127
Albuquerque, NM 87185-1127

Award Number: DE-EE0000595-1558

Project Team: Georgia Institute of Technology (Georgia Tech)
Bucknell University
King Saud University (KSU)
German Aerospace Center (DLR)

Principal Investigator: Clifford K. Ho
Distinguished Member of the Technical Staff
Phone: 505-844-2384
Email: ckho@sandia.gov

Business Contact: Shannon Boynton, Financial Administrator
Phone: 505-284-2303
Email: sboynto@sandia.gov

HQ Tech Managers: Levi Irwin (Levi.Irwin@ee.doe.gov)
Andru Prescod (Andru.Prescod@EE.Doe.Gov)

HQ Project Officer: Christine Bing (Christine.Bing@ee.doe.gov)



Executive Summary

The objective of this work was to advance falling particle receiver designs for concentrating solar power applications that will enable higher temperatures ($>700\text{ }^{\circ}\text{C}$) and greater power-cycle efficiencies ($\geq 50\%$ thermal-to-electric). Modeling, design, and testing of components in Phases 1 and 2 led to the successful on-sun demonstration in Phase 3 of the world's first continuously recirculating high-temperature 1 MW_t falling particle receiver that achieved $>700\text{ }^{\circ}\text{C}$ particle outlet temperatures at mass flow rates ranging from $1 - 7\text{ kg/s}$.

Particle receiver system. Two different receiver designs were tested on-sun: free-fall and obstructed flow [1, 2]. On-sun testing of the free-fall particle receiver design showed that the particle temperatures increased by 50 to $200\text{ }^{\circ}\text{C}$ per meter of illuminated drop length for mass flow rates ranging from $1 - 7\text{ kg/s}$ per meter of particle-curtain width and for average irradiances up to $\sim 700\text{ kW/m}^2$. Higher temperatures were achieved at the lower particle mass flow rates due to less shading. The obstructed flow design yielded particle temperature increases over $300\text{ }^{\circ}\text{C}$ per meter of illuminated drop length for mass flow rates of $1 - 3\text{ kg/s}$ per meter of curtain width for irradiances up to $\sim 1,000\text{ kW/m}^2$. Peak particle temperatures greater than $900\text{ }^{\circ}\text{C}$ were achieved with bulk particle outlet temperatures reaching nearly $800\text{ }^{\circ}\text{C}$.

The calculated thermal efficiencies were quite variable due to uncertainties in the particle mass flow rates at high temperatures. At particle outlet temperatures $>700\text{ }^{\circ}\text{C}$, the estimated thermal efficiencies of the obstructed flow design reached up to $\sim 80\%$ at particle mass flow rates of $1 - 2\text{ kg/s}$, while the thermal efficiencies of the free-fall design reached up to $\sim 70\%$ at particle mass flow rates of $\sim 5\text{ kg/s}$, with irradiance between $500 - 1000\text{ kW/m}^2$. At larger scales and higher irradiances, thermal efficiencies approaching 90% are expected based on modeling results [3]. Test results were used to validate computational models of the falling particle receiver performance at different mass flow rates, solar irradiances, and particle temperatures.

Particles. A number of commercially available ceramic particles composed of alumina, silica, and other oxides were tested to evaluate their optical properties and durability. Spherical sintered-bauxite particles were found to be the best candidate material for our application because of its high solar absorptance [4] (>0.9), resistance to abrasion and sintering at high temperatures and pressures [4, 5], and ability to be reduced to rejuvenate its solar absorptance. In addition, 140 formulations were synthesized and tested, and 11 materials maintained $>90\%$ solar weighted absorptance after 500 hours of heating in air at $700\text{ }^{\circ}\text{C}$. The 1 MW_t system deployed at Sandia used CARBO Accucast ID50 particles with a nominal diameter of $\sim 280\text{ }\mu\text{m}$. After nearly 200 hours of on-sun testing in the 1 MW_t falling particle receiver prototype, the measured packed-bed solar absorptance of the used particles (0.946 ± 0.003) was found to be statistically the same as that of the unused particles (0.945 ± 0.001) using a two-sample t-test with 95% confidence. Formation of iron oxide (hematite) on the particle surface that may change the color of the particles appeared to wear away during testing. Particle loss through attrition and wind was found to be $\sim 0.06\%$ of the average particle mass flow rate. Of the total loss, approximately 38% was due to abrasion (especially from the Olds elevator) and 62% was from loss through the aperture.

Thermal storage. The particle collection hopper used in the prototype system consists of a stainless-steel liner with layers of insulation on the outside. For larger-scale systems operating at potentially higher temperature ($\sim 1,000^{\circ}\text{C}$), studies were performed to evaluate storage systems comprised of insulating firebrick, insulating concrete, and reinforced concrete [6]. This latter design was modeled and tested at a small scale ($\sim 300 \text{ kW}_t$), and results showed that the heat loss in these systems was less than 4% per day, which corresponded to $\sim 1\%$ per day for larger-scale systems ($\sim 100 \text{ MW}_t$), with costs less than $\$15/\text{kW}_t$.

Particle/working-fluid heat exchanger. Moving packed-bed heat exchangers implementing shell-and-tube and finned shell-and-tube designs were investigated as part of this project to heat a working fluid up to $\sim 700^{\circ}\text{C}$. Tests showed that the particle-side heat transfer coefficient was limiting, but could achieve $\sim 100 \text{ W/m}^2\text{-K}$ with proper design and spacing of the tubes and fins [7]. Fluidized-bed designs were also characterized from the literature, which yielded higher particle heat transfer coefficients (up to $\sim 600 \text{ W/m}^2\text{-K}$) but with higher parasitic power consumption and heat loss associated with the particle fluidization.

Particle lift. The particle lift used in the prototype system is a stainless-steel Olds elevator that can operate at over 800°C . A cylindrical casing rotates about a stationary screw to lift particles up $\sim 8 \text{ m}$ at a variable controlled rate of up to $\sim 10 \text{ kg/s}$. Because the particles are lifted by friction between the particles and the rotating casing, the lift efficiency is low ($\sim 5\%$). For larger-scale systems, an insulated skip hoist system was designed that can achieve $\sim 80\%$ lift efficiency with a parasitic power consumption less than 1% of the rated electrical output of the CSP plant.

Path forward. The ability to achieve average particle outlet temperatures $> 700^{\circ}\text{C}$ with an on-sun 1 MW_t falling particle receiver system was successfully demonstrated. Additional testing and challenges that should be addressed in order to scale up to larger systems (e.g., $\geq 10 \text{ MW}_e$) include the following:

- Integration with a particle-to-working-fluid heat exchanger, potentially operating at high working-fluid temperatures (700°C) and pressures (20 MPa)
- Increasing receiver thermal efficiency through consideration of alternative geometries, sizes, and heat-loss reduction methods
- Reducing particle attrition and loss through higher-efficiency (low-friction) particle lifts and wind protection
- Enabling variable particle mass flow control and measurement to account for varying DNI and cloud conditions. Current test results showed that particle mass flow decreased with increasing temperature due to changes in discharge-plate slot aperture and/or particle/wall friction coefficients.

Contents

Executive Summary	2
Introduction and Background	5
Project Results and Discussion	5
Subsystem 1: Receiver	6
On-Sun Particle Receiver Design, Testing, and Modeling	6
Particle Flow through Porous Structures	18
Subsystem 2: Particles	25
Radiative properties of particles	25
Particle Durability	29
Subsystem 3: Balance of Plant	31
Thermal Storage	31
Heat Exchanger	38
Particle Lift	41
Discussion and Path Forward	43
Cost and performance comparisons	43
Scale-Up Considerations	44
Tech to Market.....	47
Conclusions.....	48

Introduction and Background

The falling particle receiver is an enabling technology that can increase the operating temperature of concentrating solar power (CSP) processes, improving efficiency and lowering the costs of energy storage [8]. Conventional central receiver technologies are limited to temperatures of around 600°C. At higher temperatures, nitrate salt fluids become chemically unstable. In contrast, direct absorption receivers using solid particles that fall through a beam of concentrated solar radiation for direct heat absorption and storage have the potential to increase the maximum temperature of the heat-transfer media to over 1,000°C. Once heated, the particles may be stored in an insulated tank and/or used to heat a secondary working fluid (e.g., steam, CO₂, air) for the power cycle. Thermal energy storage costs can be reduced by directly storing heat at higher temperatures in a relatively inexpensive medium (i.e., sand-like particles). Because the solar energy is directly absorbed in the sand-like working fluid, the flux limitations associated with tubular central receivers (high stresses resulting from the containment of high temperature, high pressure fluids) are mitigated. The falling particle receiver appears well-suited for scalability ranging from 10 – 100 MWe power-tower systems [8].

Although a number of analytical and laboratory studies had been performed on the falling particle receiver prior to this study [9-19], only one set of on-sun tests of a simple falling particle receiver had been performed [20]. Those tests only achieved 50% thermal efficiency, and the maximum particle temperature was less than 300°C. Kolb [21] and Tan et al. [22-25] discuss the use of air recirculation and aerowindows to mitigate heat loss and wind impacts in falling particle receivers, but no tests were performed. Hruby [13] introduced the concept of using ceramic objects or plates in the particle flow stream to decelerate the particles for increased heating, but no studies were conducted. This study addresses the gaps and needs identified in the previous studies.

Project Results and Discussion

This project studied all components relevant to a particle-based CSP system: (1) receiver, (2) particles, and (3) balance of plant – including thermal storage, particle heat exchange, and particle conveyance (Table 1). The following sections summarize the results of this project in each of these three subsystems.

Table 1. Subsystems and technical innovations investigated in this work.

Subsystem 1: Receiver	Subsystem 2: Particles	Subsystem 3: Balance of Plant
<i>Technical Innovations</i> 1.1 Particle Recirculation 1.2 Air Recirculation 1.3 Porous structures	<i>Technical Innovations</i> 2.1 Particle Radiative Properties 2.2. Particle Durability	<i>Technical Innovations</i> 3.1 Thermal Storage 3.2 Heat Exchanger 3.3 Particle Tower Lift/Conveyance

Subsystem 1: Receiver

The first two years of this project focused on proof-of-principle modeling and component design for the falling particle receiver. Computational modeling in the first year showed that large-scale particle receivers ($\sim 100 \text{ MW}_e$) could be designed with appropriate cavity geometries and sizes with $\sim 90\%$ thermal efficiency, particle mass flow rate $\sim 400 \text{ kg/s}$ ($\sim 30 \text{ kg/s/m}$), and a peak concentration ratio of $\sim 2,000$ suns [3]. The particles used in those simulations (and their optical properties) are the same as those used in the current testing. The use of air curtains was modeled and tested in the first two years as a means to provide protection from external wind and convective heat losses [26, 27]. Results showed that while the air curtain could provide thermal efficiency benefits at high particle temperatures ($>600^\circ\text{C}$), the air curtain could also disrupt the particle flow when the particle curtain was within a meter of the aperture. It was decided that for the small-scale on-sun prototype tests, the air-curtain would be omitted. Ultimately, two designs (free fall vs. obstructed flow) were pursued in the last phase of the project and tested on sun. The remainder of this section focuses on testing and analyses of the free-fall and obstructed flow receiver designs.

On-Sun Particle Receiver Design, Testing, and Modeling

The on-sun 1 MW_t prototype particle receiver was designed and constructed in Phases 2 and 3. On-sun testing began in July 2015 and continued through the end of the project. Figure 1 shows the system and structure used to perform on-sun testing of the falling-particle receiver designs. The system consisted of a $2 \text{ m} \times 2 \text{ m} \times 2 \text{ m}$ cavity receiver with a $\sim 1 \text{ m} \times 1 \text{ m}$ aperture on the north side where concentrated sunlight entered the receiver. The ceramic particles (CARBO Accucast ID50) were released from a top hopper above the receiver and fell through the cavity. Inside the cavity, the particles were irradiated by concentrated sunlight from a field of over 200 heliostats at the National Solar Thermal Test Facility at Sandia National Laboratories. The heliostat field is capable of generating up to 6 MW of thermal energy. After falling through the receiver, the particles were collected in a bottom hopper and funneled into a high temperature Olds particle elevator that lifted the particles inside a rotating casing surrounding a stationary auger. The particles were discharged into the top hopper, where the particles were released into the cavity receiver. The mass flow rate of particles falling into the receiver was controlled by a fixed slot aperture in a discharge plate at the base of the top hopper [28]. The receiver system also included a water-cooled flux target with a Kendall radiometer that was used to measure and characterize the concentrated irradiance distribution from the heliostat field. The receiver system was instrumented with over 150 thermocouples to record temperatures throughout the system. At the base of the receiver, the particles flowed through five funnels spaced evenly apart that allowed the particles to accumulate within the funnels and immerse a thermocouple to measure the particle outlet temperature after being heated in the receiver.

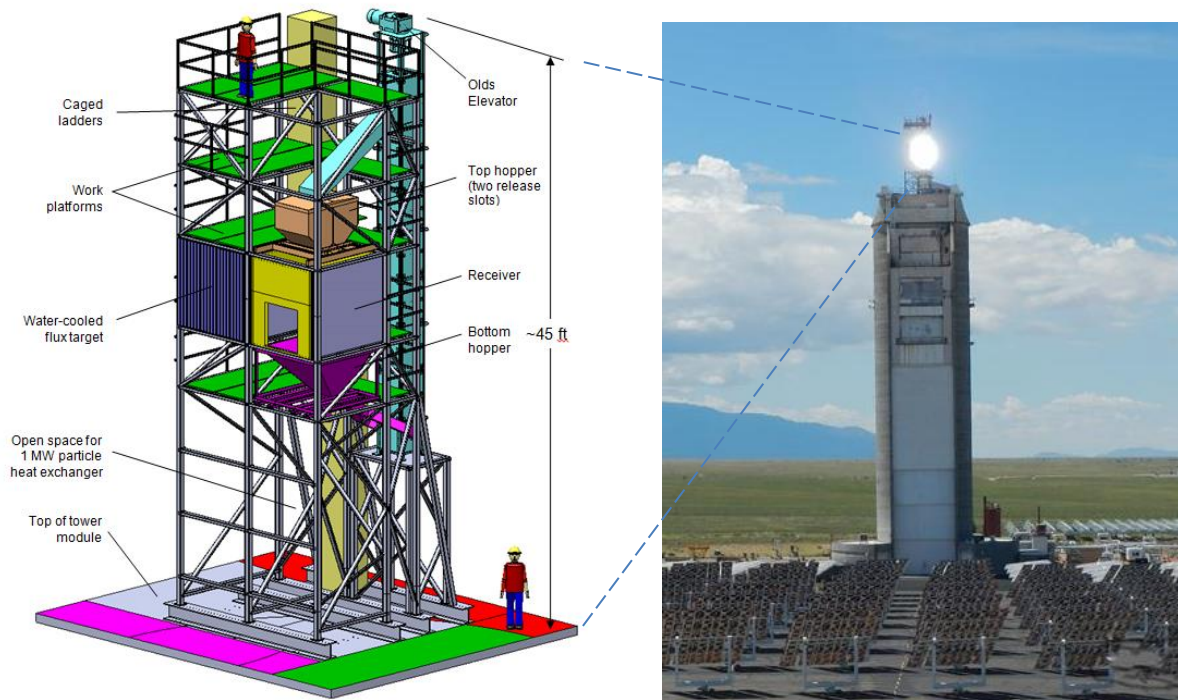


Figure 1. On-sun falling particle receiver prototype system.

Free-Fall Particle Receiver Design

In the free-fall particle receiver design, the particles flowed through one of two available discharge hoppers above the receiver (Figure 2, left). A diverter valve was used to direct the particle flow to either of the hoppers. A slotted discharge plate at the base of the hopper distributed the particles uniformly along a straight line into the receiver. Different sized slot apertures were used to investigate the impact of different mass flow rates [28]. Due to thermal expansion of the stainless steel plates that were used in early tests, which changed the particle mass flow rates as the temperatures increased (to $\sim 700^\circ\text{C}$), ceramic discharge plates were machined and used in the free-fall tests. Ho et al. [28] describe the characterization of the particle flow (velocity, opacity, curtain thickness, bulk density) as a function of the particle mass flow rate, which ranged from $\sim 1\text{ kg/s} - 7\text{ kg/s}$ per meter of slot length.

Obstructed-Flow Particle Receiver Design

The receiver design is shown in Figure 2 (middle) and consisted of a staggered array of stainless-steel SS316 chevron-shaped porous mesh structures affixed onto an insulating alumina board ($\sim 1.2\text{ m}$ high x 1.2 m wide) placed inside of the cavity receiver under the front (north-most) discharge hopper. The particles flowed through a discharge slot at the base of the hopper and into the receiver. Several discharge slots were attempted ($1/4''$, $3/8''$, and $7/16''$), but it was found that the larger slot apertures produced a waterfall effect that caused particles to flow in front of the mesh structures and miss the thermocouple funnels below. So, only the $1/4''$ slot aperture data were

used. Inside the receiver, the particles flowed through and over the chevron-shaped mesh structures (similar to a Pachinko board) as they were irradiated by the concentrated solar flux entering through the aperture [29, 30]. The intent of the structures was to slow the particles and increase the residence time within the concentrated flux.

Figure 2 shows an image of the particles flowing through and around the chevron-shaped mesh structures. As described in Ho et al. [2, 28], the mesh structures reduced the terminal velocity of the particles by nearly an order of magnitude from $\sim 5 - 6$ m/s to $\sim 0.5 - 0.8$ m/s at 1 – 2 meters of drop length. The depth of the chevrons was ~ 13 cm, and the slot from the discharge plate was centered over the chevrons. Although most of the chevron surface was covered by flowing particles, the leading edge (2 – 4 cm) was still visible and exposed to direct irradiance (Figure 2). In addition, the particle mass flow rate in the center of the receiver (where the irradiance was greatest) was reduced due to thermal expansion and buckling of the discharge plates, which narrowed the discharge slot aperture near the center. This led to overheating, oxidation and failure of the mesh structures as shown in Figure 3 (left image) [1]. We later installed a smaller mesh insert that consisted of four different mesh materials (SS316, Inconel 601, Hastelloy X, and Hastelloy C276) for on-sun testing to determine which materials might be suitable (Figure 3, middle and right). Testing of additional mesh materials was performed by Georgia Tech (see *Mesh Durability Testing*).

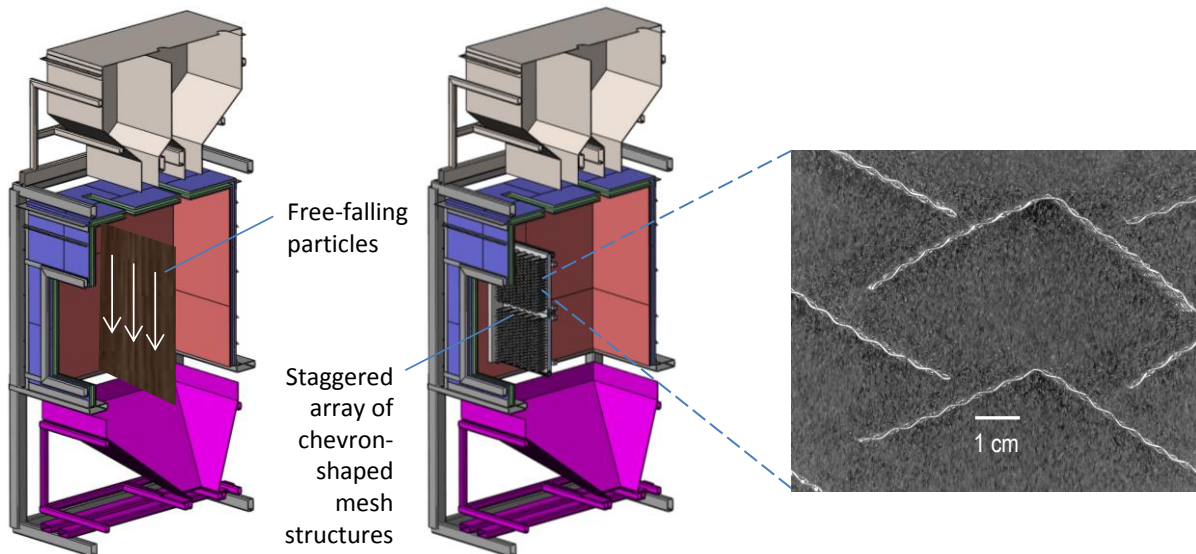


Figure 2. Cutaway illustration of free-falling (left) and obstructed-flow (middle and right) particle receiver designs.

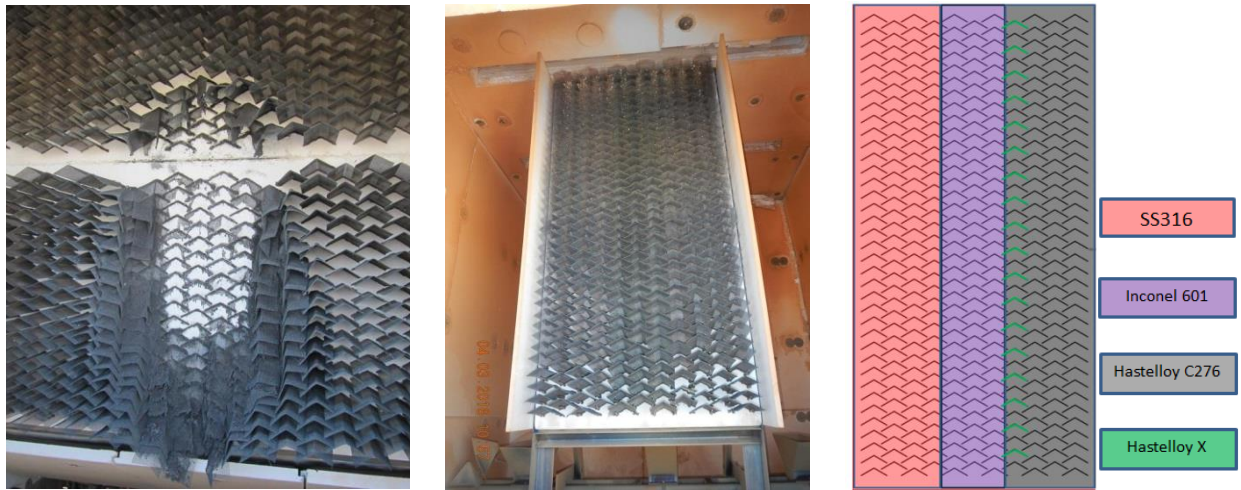


Figure 3. Original (left) and new (middle & right) mesh inserts for obstructed-flow tests.

Test Approach

A series of on-sun tests were performed to evaluate the two receiver designs with the continuously recirculating falling particle receiver system. In each test, heliostats were selected to provide a desired irradiance on the receiver. The irradiance distribution on the receiver was characterized by using photographic images of the combined heliostat beams on the water-cooled flux target adjacent to the receiver (Figure 4). The irradiance on the flux target was photographed, and a Kendall radiometer located in the center of the flux target provided an irradiance measurement that was used to scale the pixel values. The ray-tracing tool SolTrace was used to identify heliostat configurations that would produce a desired peak flux and power into the receiver. The residence time of the particles in the concentrated beam of light was approximately 0.2 – 0.4 s for the free-falling design and 1 – 3 s for the obstructed flow design based on measured velocities and the height of the illuminated region.

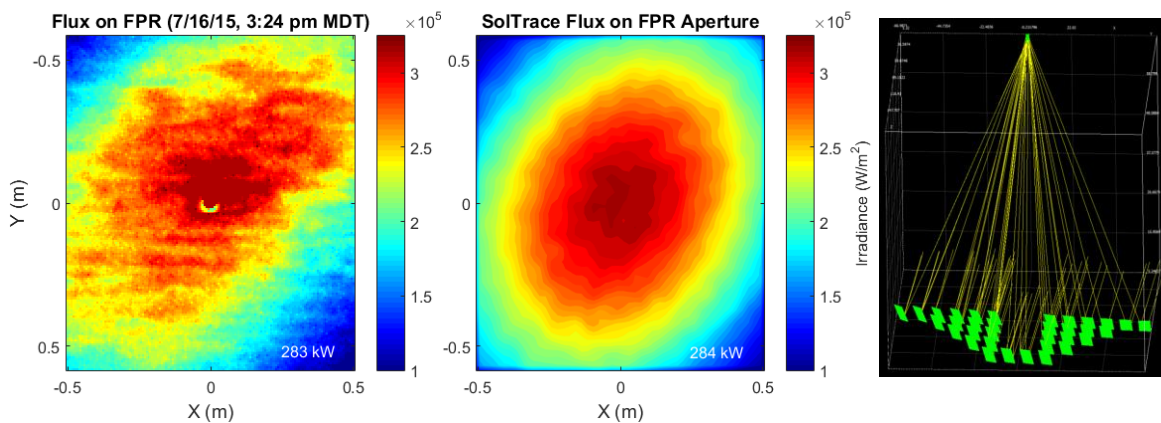


Figure 4. Measured (left) and simulated (middle) irradiance distributions on the flux target using SolTrace (right) with a peak flux of $\sim 300 \text{ kW/m}^2$ from 34 heliostats at 15:24 MDT on July 16, 2015.

Thermocouples were used to measure the particle temperatures at several locations at the inlet and outlet of the receiver. The power absorbed by the particles was determined by the particle mass flow rate, specific heat, and inlet and outlet temperatures. The thermal efficiency was determined as the ratio of the absorbed power to the incident power:

$$\eta_{th} = \frac{Q_{abs}}{Q_{in}} = \frac{\dot{m}(h_{out} - h_{in})}{Q_{in}} = \frac{\dot{m} \int_{T_{in}}^{T_{out}} c_p(T) dT}{Q_{in}} = \frac{\dot{m} \left[\frac{365}{1.18} (T_{out}^{1.18} - T_{in}^{1.18}) \right]}{Q_{in}} \quad (0)$$

where Q_{abs} is the power absorbed by the particles (W), h is the enthalpy of the particles (J/kg), \dot{m} is the particle mass flow rate, Q_{in} is the incident power on the particles, and T_{in} and T_{out} are the inlet and outlet particle temperatures, respectively. In Eq. (0), the following relation [28] derived from measured data for the particle specific heat as a function of temperature (in degrees Celsius) was used:

$$c_p(T) = 365T^{0.18} \quad (0)$$

The following protocol was implemented during the tests: (1) turn on the particle elevator to begin particle flow through the system; (2) aim the prescribed heliostats at the water-cooled flux target and measure the irradiance; (3) aim the heliostats at the receiver aperture and heat the particles to a desired (bulk) temperature entering the receiver; (4) at the desired temperature, remove the heliostats and allow the particles to mix and temperatures to stabilize; (5) aim the prescribed heliostats at the receiver aperture to heat the particles and allow temperatures to stabilize for several minutes; (6) aim heliostats at water-cooled flux target and measure irradiance; (7) repeat steps (3) – (6) as necessary to evaluate particle temperature rise and thermal efficiency at different temperatures.

Free-Fall On-Sun Test Results

Figure 5 shows the increase in particle temperature per unit drop length and the thermal efficiency as a function of the average irradiance for the free-fall particle receiver tests. In these tests, different slot apertures were used to produce different particle mass flow rates. In the plots, the results are categorized between low-flow (~1 – 3 kg/s/m) and high-flow (~3 – 6 kg/s/m) conditions. The mass flow is reported per unit length of the slot to normalize tests where the slot lengths were different. For the early high-flow cases (before we replaced the diverter valve with a larger duct in Jan 2016 to handle higher particle mass flow rates), the slot had to be reduced to accommodate the limited particle mass flow through the diverter valve and discharge chute (~4 kg/s).

Average particle outlet temperatures¹ during the free-fall tests exceeded 700 °C at its hottest, and peak temperatures exceed 800 °C. Results show that the average particle temperature rise ranged from ~50 – 125 °C/m for average irradiances of ~200 - 400 kW/m² to 150 – 225 °C/m for average irradiances of ~500 - 700 kW/m² at low flow rates. At the higher particle flow rate, the average particle temperature rise was less due to the

¹ Average particle outlet temperatures are different than the “Average Particle Temperatures” labeled in Figure 5, which represent the average particle temperatures between the inlet and outlet.

increased thickness and opacity of the particle curtain, which created additional shading, but the average particle temperature rise was still nearly $\sim 75 - 100$ °C/m for average irradiances approaching 700 kW/m^2 . The thermal efficiency ranged from 0.4 – 0.7 for the lower irradiances and increased to 0.5 – 0.8 at the higher irradiances. Surprisingly, the thermal efficiency was not strongly correlated to the particle mass flow rate in the measured data. We expected that the thermal efficiency would increase with increased mass flow rate due to a more opaque curtain and greater light interception and absorption. Possible factors that could confound the results include transient (non-steady) conditions during the heating tests and inaccurate mass flow estimates as a function of temperature.

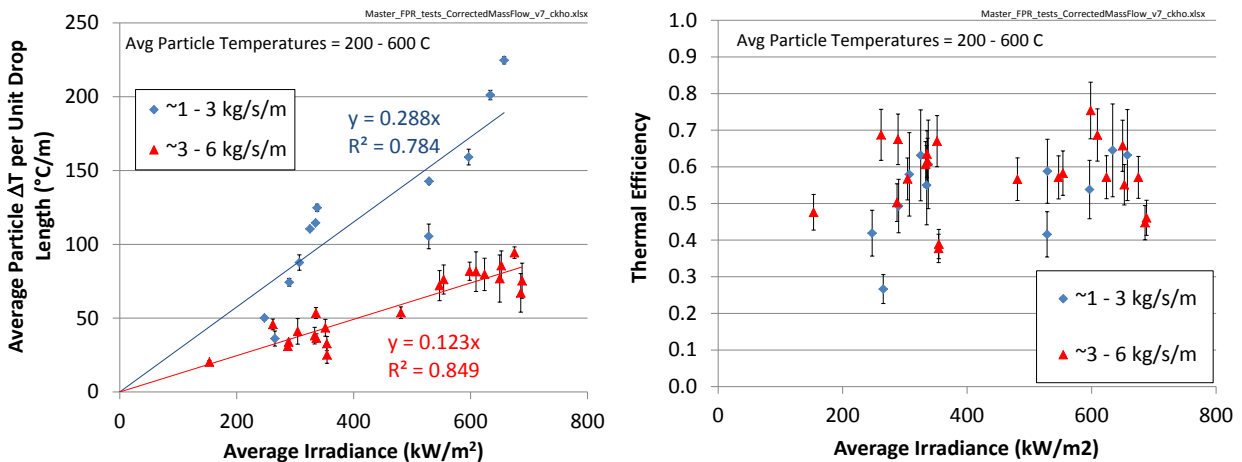


Figure 5. Measured increase in particle temperature (left) and thermal efficiency (right) as a function of average irradiance for the free-fall receiver design. Error bars represent one standard deviation.

CFD Modeling of Free-Fall Tests

Twelve computational fluid dynamics (CFD) simulations of representative test cases were performed for comparison and validation. A discrete ordinates radiation model in ANSYS Fluent was used to model the coupled solar irradiance, scattering, reflection, thermal emittance, convection, turbulence, and discrete-phase particle flow and heat transfer [31]. The simulated cases contain a combination of low and high values for irradiance, particle inlet temperatures, and particle mass flow rates. Table 2 summarizes the boundary conditions and parameters from the tests that were used in the model.

Table 2. Summary of simulated test cases.

Case	Test Date	Nominal Slot Aperture (in)	Particle Mass Flow Rate (kg/s/m)	Particle Inlet Temperature (C)	Incident Power on Aperture (MW)
1	2/26/2016	1/4	1.42	520	0.50
2	2/26/2016	1/4	1.62	438	0.99
3	2/26/2016	1/4	1.68	412	0.48

Case	Test Date	Nominal Slot Aperture (in)	Particle Mass Flow Rate (kg/s/m)	Particle Inlet Temperature (C)	Incident Power on Aperture (MW)
4	2/26/2016	1/4	1.85	340	0.95
5	3/10/2016	3/8	3.38	640	0.50
6	2/25/2016	7/16	3.45	663	0.52
7	3/10/2016	3/8	3.50	581	1.02
8	2/25/2016	7/16	3.70	610	0.82
9	2/25/2016	7/16	4.13	519	0.43
10	3/10/2016	3/8	4.13	266	0.83
11	3/10/2016	3/8	4.44	111	0.40
12	2/25/2016	7/16	4.69	400	0.91

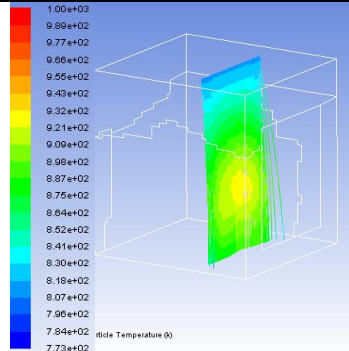
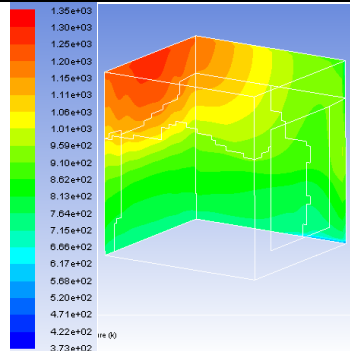
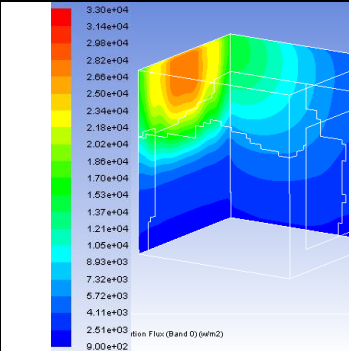
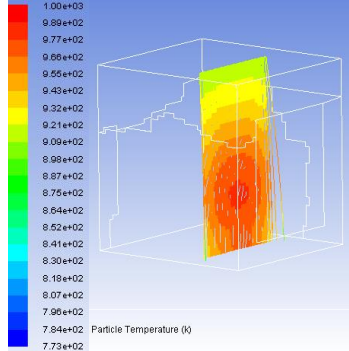
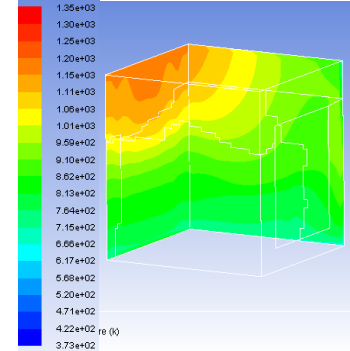
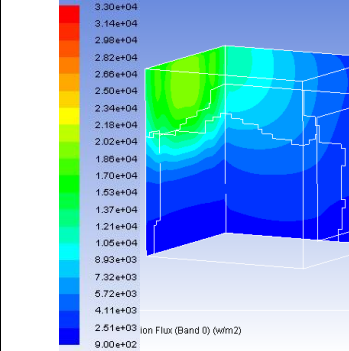
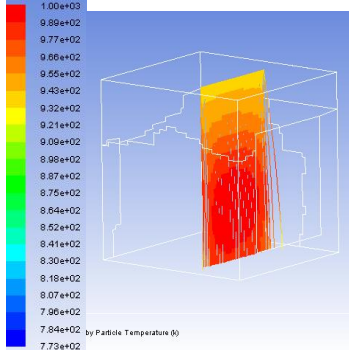
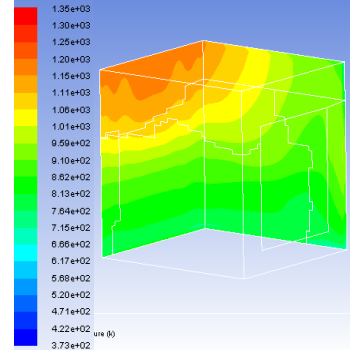
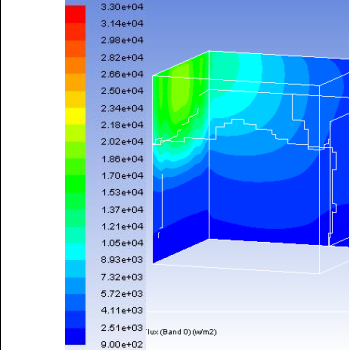
Table 3 shows simulated results from three representative cases. The particles are plotted as traces colored by temperature. The back wall and west wall are seen with two different contour plots detailing the temperatures of the walls and absorbed irradiance (<4.5 microns, which was the band in which the incident solar radiation was applied). Increased particle mass flow results in an increase in particle curtain opacity which is a key design consideration for both thermal efficiency and wall protection. Thicker curtains result in lower irradiance values on the walls behind the curtain and 100-200 °C cooler temperatures. However, thicker curtains also result in lower particle temperature rise due to increased shading.

Figure 6 shows plots of the simulated vs. measured results for particle temperature rise and thermal efficiency for the 12 cases. The predicted particle temperature rise is within $\pm 20\%$ of the measured values and does not show a clear trend of over predicting or under predicting. The predicted thermal efficiencies show a much broader range (with less uncertainty) than the corresponding measured values for the boundary conditions considered. Primary reasons for the discrepancy include measurement uncertainties in the particle mass flow rate, which changed with increasing temperatures, and to a lesser degree prediction uncertainties in the irradiance distribution and directionality.

Obstructed-Flow Test Results

Average particle outlet temperatures during the obstructed-flow tests reached nearly 800°C at its hottest, and peak temperatures exceed 900 °C. Figure 7 shows the increase in particle temperature per unit drop length and the thermal efficiency, respectively, as a function of the average irradiance for the obstructed-flow particle receiver tests (Figure 3). The values were recorded for average particle temperatures of ~500 °C – 700 °C and particle mass flow rates of ~1.5 – 2.5 kg/s/m (1/4" RSLE slot). Results show that the average particle temperature rise ranged from ~50 °C/m for average irradiances of ~100 – 200 kW/m² to 150 – 200 °C/m for average irradiances of 300 – 400 kW/m². At average irradiances of 600 – 1000 kW/m², the average particle temperature rise ranged from 300 – 350 °C/m. The thermal efficiency ranged from ~0.5 – 0.7 for the lower irradiances to ~0.6 - 0.8 for the higher irradiances.

Table 3. Representative results from CFD simulations.

Parameters and Results	Particle Traces Colored by Temperature (K)	Back Wall and West Wall Temperatures (K)	Back Wall and West Wall Absorbed Irradiance (< 4.5 microns) (W/m ²)
<ul style="list-style-type: none"> 6.35 mm Aperture Size 1.60 kg/s Irradiance on Aperture=500 kW_t Inlet Temperature = 520°C Avg. Outlet Temperature = 608°C Temperature Rise (C/m) = 73 Overall Thermal Efficiency = 26% Particle Curtain Efficiency = 31% 			
<ul style="list-style-type: none"> 9.5 mm Aperture Size 3.38 kg/s Irradiance on Aperture=500 kW_t Inlet Temperature = 640°C Avg. Outlet Temperature = 681°C Temperature Rise (C/m) = 35 Overall Thermal Efficiency = 35% Particle Curtain Efficiency = 42% 			
<ul style="list-style-type: none"> 11.1 mm Aperture Size 3.82 kg/s Irradiance on Aperture=520 kW_t Inlet Temperature = 663°C Avg. Outlet Temperature = 706°C Temperature Rise (C/m) = 36 Overall Thermal Efficiency = 38% Particle Curtain Efficiency = 45% 			

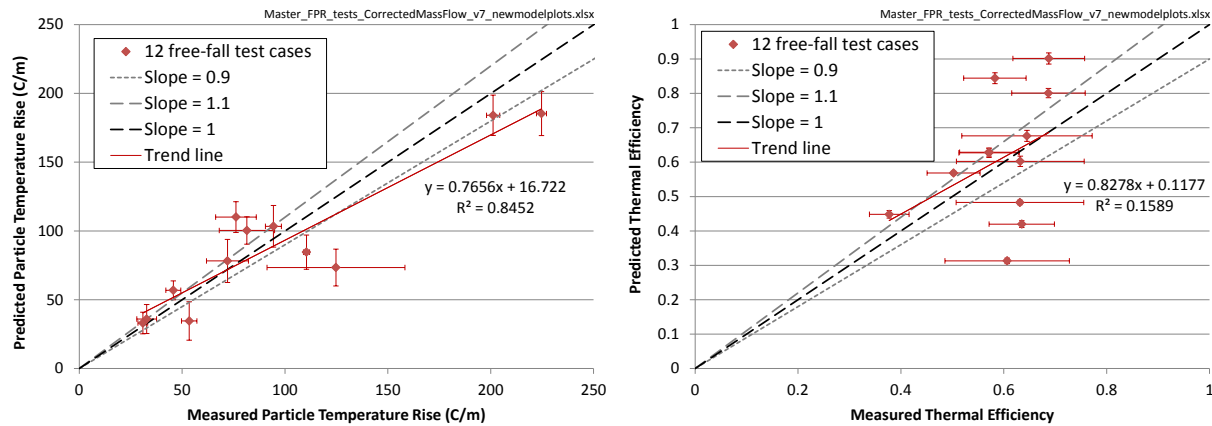


Figure 6. Simulated vs. measured results for particle temperature rise (left) and thermal efficiency (right) for the free-fall cases. Error bars represent one standard deviation.

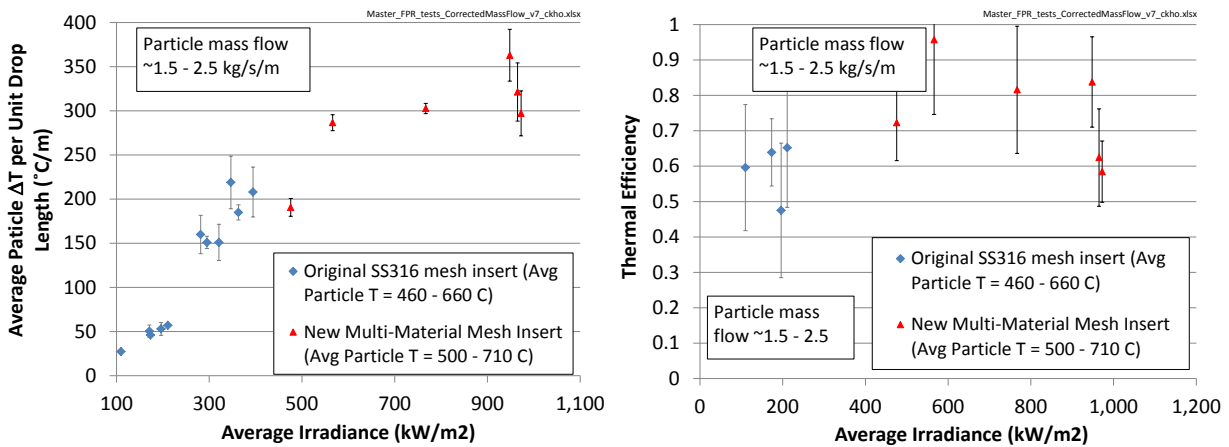


Figure 7. Measured increase in particle temperature (left) and thermal efficiency (right) as a function of average irradiance for the obstructed-flow receiver design. Error bars represent one standard deviation.

In general, the average particle temperature did not show a strong correlation to the particle temperature increase or the thermal efficiency. The particle temperature rise per unit drop length was greater for the obstructed-flow design due to the increased residence time of the particles in the concentrated sunlight. The thermal efficiency of the obstructed-flow design was generally higher as well for the irradiances tested (Figure 8). We believe that the slower particle velocities in the obstructed-flow design reduced convective heat losses and flow instabilities of the particles observed in the free-fall tests.

Although the estimated thermal efficiencies of the tests did not show strong correlations to most input parameters due to measurement uncertainties, the simulated thermal efficiency for the free-fall cases was used to determine rank-regression coefficients for the input parameters to quantify the most important parameters impacting thermal efficiency and particle temperature rise. Figure 9 shows that the particle mass flow rate

and particle inlet temperature had the strongest influence on simulated thermal efficiency, while incident power, particle mass flow rate, and particle inlet temperature had the largest impact on particle temperature rise.

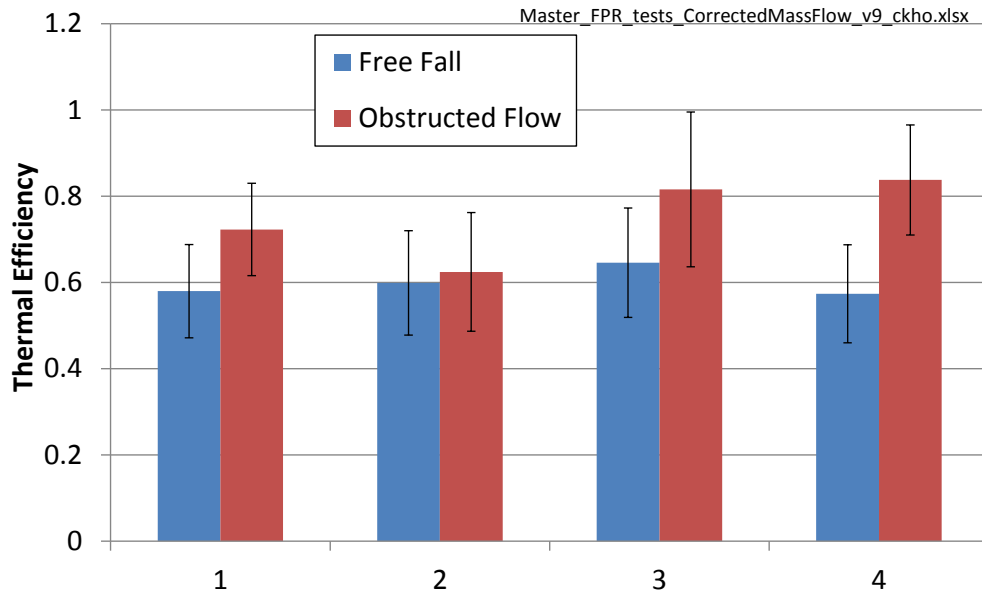


Figure 8. Thermal efficiency comparisons for comparable tests with similar mass flow, irradiance, and inlet temperatures.

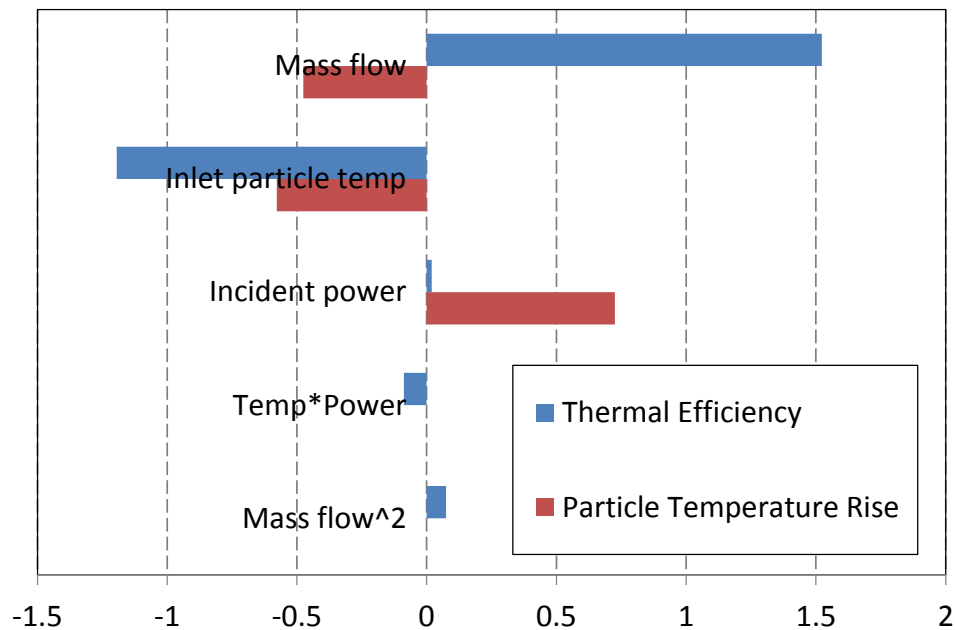


Figure 9. Rank-regression coefficients of various input parameters corresponding to simulated thermal efficiency and particle temperature rise of the free-fall cases.

On-sun mesh durability evaluation

As discussed in earlier reports [1], oxidation of the SS316 wires in the original mesh insert led to its catastrophic failure (Figure 3, left; Figure 10). In deteriorated locations, the stainless steel melted and leaked out of the chrome oxide shell (Figure 10, right), leaving behind a hollow, brittle wire that crumbled when handled.

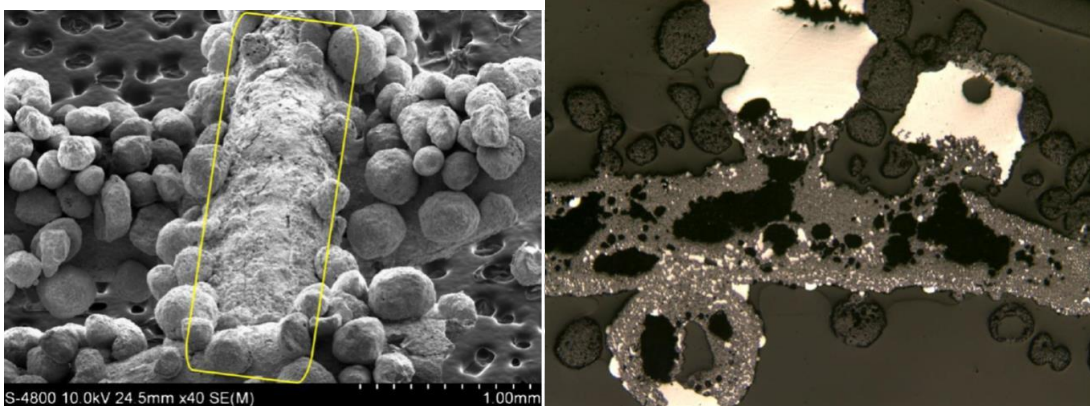


Figure 10. Images of mesh failure. Left: SEM image of particles sintered onto mesh. Right: image of cross-section of oxidized mesh (white is stainless steel, rough gray area is oxidized mesh).

The new multi-material mesh insert was tested on-sun over several days for over 14 hours, experiencing well over 1000 suns during the tests. Samples of each of the four materials were analyzed using SEM and EDS. Table 4 shows images of the four samples, illustrating the damaged areas. The Hastelloy C276 experienced the most apparent damage, with the leading edge of the mesh receding 4 – 5 cm from its original length due to direct exposure from the incident irradiation. The SS316 also experienced some damage near the leading edge, while the Inconel 601 and Hastelloy X experienced the least amount of damage. SS316 showed the greatest signs of oxidation, and Inconel 601 and Hastelloy C276 showed the least signs of oxidation. Hastelloy X showed some signs of defects, but no significant oxidation. Overall, the Hastelloy X and Inconel 601 appeared to perform the best, but all four materials showed some signs of wear or deterioration.

Challenges encountered during the on-sun tests

Challenges encountered during the on-sun tests included thermal expansion of the discharge plates, which reduced the slot aperture and particle mass flow rate near the center of the slot. This effect was noted initially for the stainless steel plates, but we found that reduction in the aperture was also observed in the RSLE plates, despite the very low coefficient of thermal expansion ($0.3 \times 10^{-6}/^{\circ}\text{C}$). This was determined by measuring the slot aperture after the tests and measuring the discharge time for the particle inventory to determine the reduced mass flow rate at different particle temperatures.

Table 4. Images of four materials tested on-sun in the multi-material mesh insert.

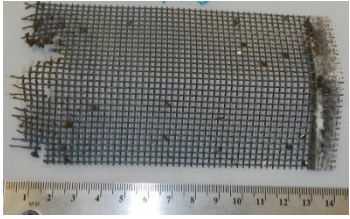
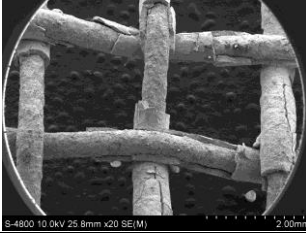
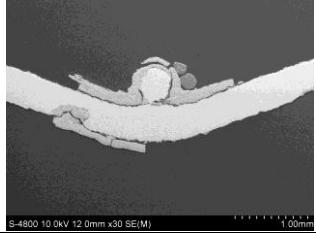
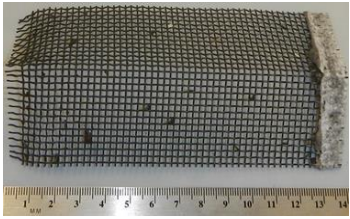
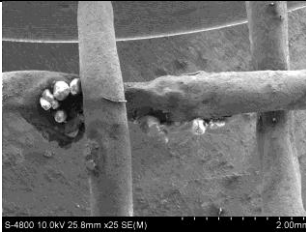
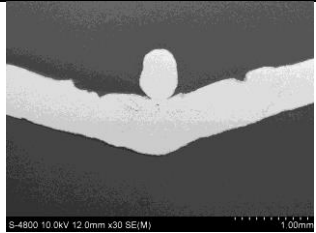
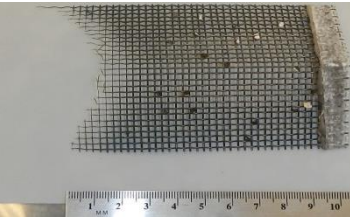
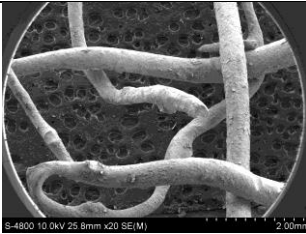
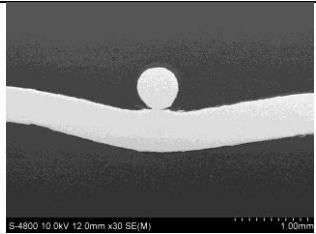
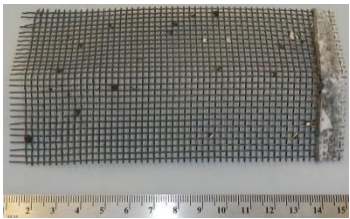
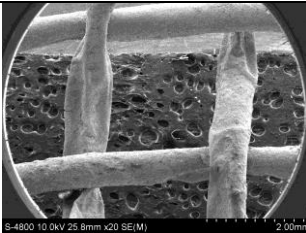
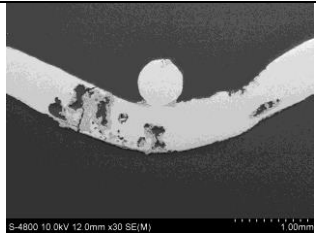
Material	Mesh Sample Pulled from Insert (left edge faced incident irradiation)	SEM Image of Damaged Interwoven Wires	SEM Cross Section
SS316			
Inconel 601			
Hastelloy C276			
Hastelloy X			

Figure 11 shows the measured ambient particle mass flow rates as a function of the RSLE slot aperture (left plot). Figure 11 also shows a plot of the estimated mass flow rate of particles as a function of particle temperature flowing through the discharge plate. The ratio of the particle discharge times (to completely empty the top hopper when full) was used to determine the mass flow rate at different temperatures assuming the particle inventory was the same in each test. It appears that particle flow through the RSLE discharge plates is about 5 – 20% less than the particle flow through steel discharge plates with equivalent apertures.

The particle flow is lower at higher temperatures due, in part, to narrowing of the RSLE aperture slot at higher temperatures. The apertures were measured after each heating test, and although the change was much less than the steel plates, the initial “1/4-inch” slot decreased by ~6% (compared to 30% for the stainless-steel plates), which would cause a decrease in the mass flow rate by ~10% according to the Beverloo equation. The initial “3/8-inch” and “7/16-inch” RSLE plates changed less (by ~2%). We also postulate that the RSLE plate is rougher than the machined steel plates, and the friction

factor is greater, causing the particles to flow less easily through the RSLE slot. In addition, test results from Jenike & Johanson revealed that the friction between the particles and steel walls increased by up to 70% when temperatures increased from 22°C to 600°C, depending on the wall material. This could also cause additional reduction in particle mass flow through the discharge plate slots. Interestingly, Jenike & Johanson found that the internal particle friction decreases with increasing temperature (~17% from 22°C to 600°C). So, flow of particles over other particles will be increased at higher temperatures (lower effective viscosity, like honey), but the flow of particles next to walls will be less. This will have an impact on particles flowing through ducts, slots, and openings in various components such as the hoppers, mesh structures, and particle heat exchangers.

The development of real-time control and measurement of particle mass flow is strongly recommended for future studies and any commercial particle receiver system.

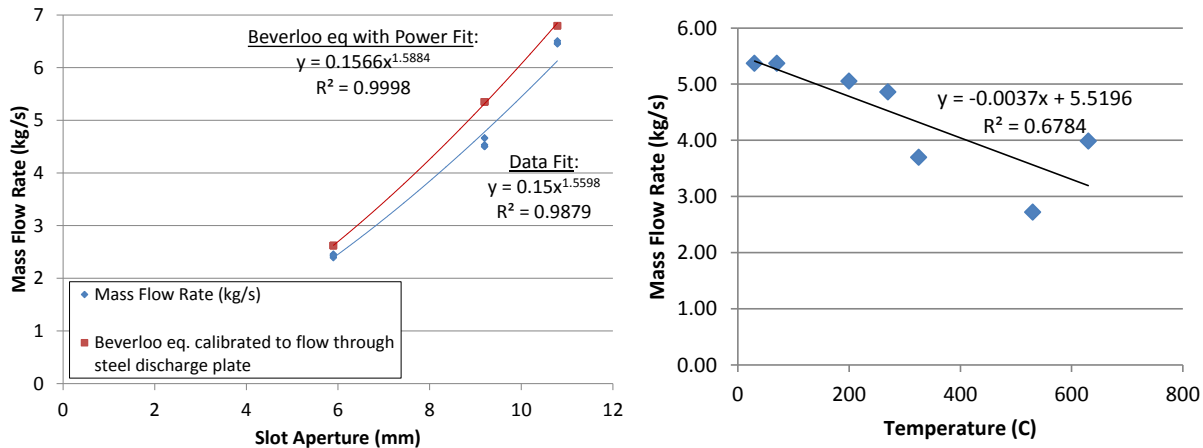


Figure 11. Left: Measured mass flow rate through RSLE discharge plates with three different aperture sizes used in the tests (5.9, 9.2, and 10.8 mm). Right: Estimated mass flow as a function of temperature for the 9.2 mm aperture RSLE plate.

Particle Flow through Porous Structures

This section summarizes work performed by Georgia Tech to evaluate particle flow and heat transfer through porous structures. The goal of these studies was to provide data and information to aid in the design of the obstructed-flow insert that was used in the on-sun tests described in the previous section. Initial evaluations included studies of flow and clogging in porous ceramic foams in Phase 1 [32-35]. The following sections focus on the porous mesh structures designed and evaluated in Phases 2 and 3.

Discrete Porous Structure Durability Testing

Durability testing of stainless steel, tungsten, and several high temperature alloys was completed in Phase 2 using the high temperature hour glass device to abrade the meshes with particulate. All high temperature alloys passed the testing including a promising iron/chromium/aluminum alloy. This testing had successfully identified the

SS316 alloy used in the initial panel for SNL testing. The results of this testing have been reported in a conference presentation [36] and has generated one Masters thesis [36].

Georgia Tech High Flux Solar Simulator (GTHFSS) Testing

Preliminary experiments were conducted using the GTHFSS during Phase 1 and 2 with a low temperature recirculating apparatus using a small OLDS elevator for particle transport. Two receiver designs spanning the range of practical alternatives were tested: a simple free-falling curtain and the chevron wire mesh design. Useful qualitative results were obtained. In Phase 2 much effort was invested in developing a new single-pass batch-type high temperature test apparatus for the GTHFSS. The batch-type apparatus has significant limitations, but was the only identified design known at that time that could operate at the very high temperatures needed and fit into the confines of the GTHFSS enclosure. The batch apparatus had the advantage that a weighing box can be used to monitor the mass flow rate. Ultimately, a calibrated scale base with a load cell has been used to measure the accumulated particulate mass with high accuracy, and this device has been invaluable in mass flow measurements in the upgraded PHR test systems. Indeed the new recirculating flow system uses a modification of this weighing box to periodically sample the mass flow in the continuous flow loop providing a feasible solution to the demanding problem of measuring mass flow of particulate streams.

Particulate Flow, Heat Transfer, and Efficiency Modeling

The issues related to CFD modeling of flow addressed in Phase 1 were extensively addressed in the special report entitled "Modeling of Particulate Flow through Interconnected and Discrete Porous Structures" which was submitted to the DOE on August 16, 2013. Model development and investigations during Phase 2 have been described previously in the continuation report and in two specific publications [37] and [38]. In summary, two CFD-based Finite Volume Method (FVM) approaches implemented in Fluent have been pursued (1) an Euler-Euler (E-E) method desirable for its inherent numerical efficiency and (2) an Euler-Lagrangian (E-L) formulation which allows simulation of individual particles by the Discrete Element Model (DEM). This E-L approach is computationally intensive but necessary for simulation of all the critically important thermal and mechanical processes in a particle receiver: absorbed radiation, heat transfer and loss, particle-particle and particle-mesh interactions, and ultimately solar energy collection. Simulations of dense flows discrete particles are very computationally intensive and time consuming preventing much practical use with existing simulation technology. Nevertheless, some useful results were obtained. Most importantly, the simulations indicated that collection efficiencies as high as 92% at 700°C might be feasible at 1000 suns (or higher) concentration. Furthermore, modeling showed agreement with experiments on particle velocities, overall mass flow rates, and the formation of a low relatively dense layer on the wire meshes. These simulations have successfully supported the understanding of the particulate flow, mesh configuration, and overall design.

Cost and Fatigue Analysis of Discrete Structure Porous Heating Receiver (DSPHR)

During Phase 2, a preliminary design of a large commercial scale DSPHR was developed for cost and fatigue modeling. This DSPHR design is a series of 0.61 m by 1.22 m wide high temperature insulating board panels supporting the refractory metal meshes. The panels are connected to a lightweight structural steel frame by a series of struts. High temperature insulation protects the frame and minimizes heat losses. Obviously, this can be a relatively low cost and lightly loaded design with the light loading contributing to low cost and quick start up.

A preliminary cost estimate was prepared and presented assuming 1.0 MWth/m² irradiation and 90% efficiency resulting in an estimated bare cost of around \$6 per kW-thermal; consequently, the cost of the DSPHR panel will be small relative to the combined target cost of the receiver and tower (\$150/kW_{th}).

Fatigue Analysis. The proposed structure is by design largely immune to thermally induced stress because (1) the steel struts can expand outward freely when heated during startup without imposing any stress on the insulating board panels, and (2) any expansion of the panels will be minimal and easily accommodated by some minimal expansion space between panels. The only remaining cycling loads are the loads imposed on startup when particulates accumulate on the meshes and begin to impact and load the meshes, and these loads were found to be minimal; consequently, the cycling loads are predicted to be small, and fatigue failure will not be an issue.

Phase 3 Solar Simulator PHR Efficiency Testing

Testing at high temperatures in the GTHFSS was accomplished in Phase 3. The initial batch type system and an upgrade were used followed by a more advanced continuous flow system. The efficiency tests were proceeded by some qualifying tests described next followed by a summary of the efficiency testing and results.

Particle Mass Flux Characterization for GT HFSS Experiment

For consistency between the large scale tests and small scale simulator tests, the particle mass flux rate into the PHR cavity is targeted to be between 65 and 75 kg/m²-s. To ensure steady operation during efficiency testing, the R-squared for a linear regression of mass on time was specified to be > 90%. Both these criteria were surpassed in this Phase 3 Q1 testing as reported earlier.

Irradiance from GT HFSS Solar Simulator Entering Aperture

The water cooled calorimeter was refined in Q1 of Phase 3 and used to measure the concentrated flux in the GTSS to demonstrate flux densities in two desired ranges: (1) > 50 W/cm² and (2) > 100 W/cm². Standard EPA calculates uncertainties in this critical measurement low enough to support combined uncertainties in the overall PHR efficiency that will be less than 4%. Ultimately this low level of uncertainty was achieved as documented in [39]. Overall, the tests indicate that the solar flux from two lamps is greater than the 50 W/cm² project target, while three lamps nearly reach 100 W/cm², and four lamps easily exceed the 100 W/cm² solar flux goal.

Thermal Efficiency and Related Testing

As reported earlier the Georgia Tech High Flux Solar Simulator (HFSS) was used in Phase 3 Q2 to test the small scale PHR, and at lower temperatures the efficiency values appeared to be reliable and above the target value of 90%. As explained in the quarterly report, the batch apparatus was not able to provide uniform temperature to particle flow to the test PHR at higher temperature, so it was modified to include an air conveyor in the upper hopper to uniformly premix the heated particulate. This modification allowed higher temperature testing in the following quarter at temperatures in the range of 500°C up to 700°C. This experience demonstrated a feasible high temperature pneumatic conveyor system that was later adapted to allow continuous operation in ongoing Phase 3 Q5 testing. The lower temperature testing is described in a conference presentation [40].

In Q4, high temperature tests were successful in showing operation of the discrete structure PHR (DS-PHR) at the target upper temperature with particulate leaving the receiver above 700°C and with peak flux over 1000 kW/m². Visual inspection of the SS316 meshes after testing revealed no evidence of degradation under these severe conditions, but the duration of the tests was on the order of minutes, significantly shorter than the duration of the on-sun tests at Sandia. In addition, the particle mass flow rates in the solar-simulator tests was significantly less, which may have mitigated the wear and deterioration of the mesh structures relative to the on-sun tests.

The target receiver collection efficiency of 90% at high temperature has been approached, but not yet measured directly. This testing was described in a conference presentation [41], and the related uncertainty analysis has also been presented [39]. The efficiency testing was found to be overly limited by the batch apparatus, so most effort during the balance of the project was invested in developing and operating a continuous flow test system for use near the end of the project. As illustrated below, the testing at 500°C measured near steady-state efficiencies in the range of 80% to 85%. Unfortunately, the particulate supply is exhausted before a higher temperature test reaches a fully steady state condition. Consequently, the 700°C tests were not able to achieve even approximately steady temperatures in the mixer, which is downstream of the PHR. Nevertheless, inspection of the available 700°C data indicate that efficiencies somewhat lower but not drastically lower than the 500°C values might have been achieved at 700°C. All of the project objectives that can be achieved with a batch device in the GT-HFSS have been reached, and current research and testing is using the continuous flow system.

The 500°C tests were run first since this temperature, being the anticipated average receiver operating temperature, is especially important. The relevant results as steady state operation is approached are shown in Figure 12.

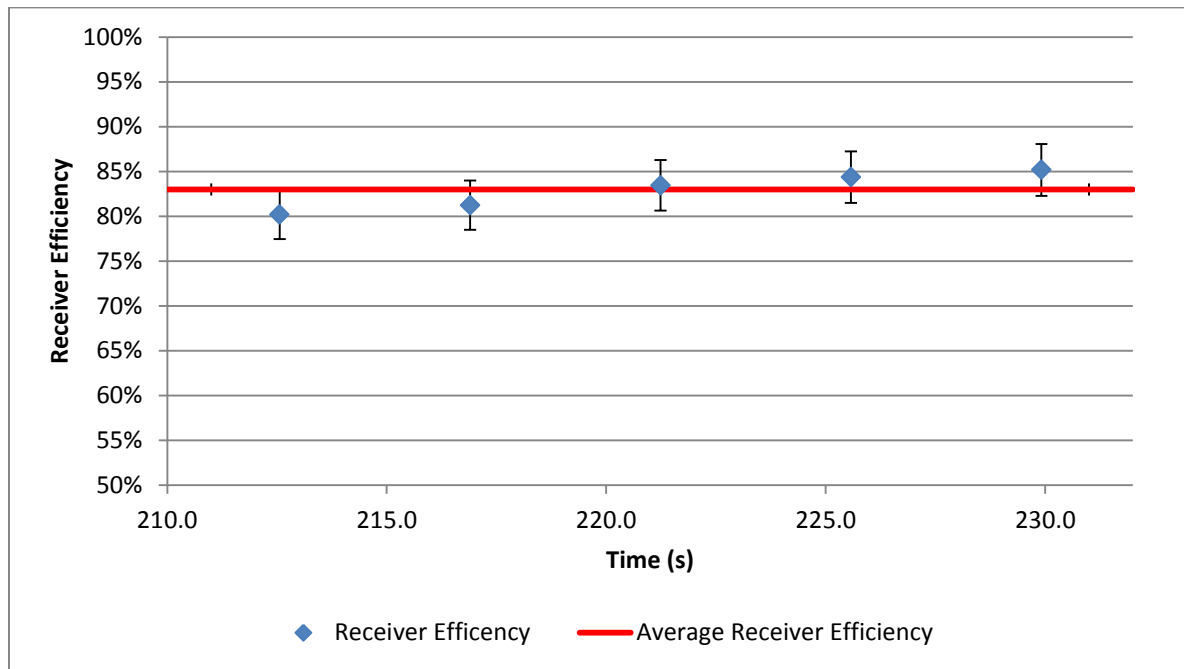


Figure 12. Efficiency results near 500°C outlet from batch apparatus in GT HFSS

Phase 3 Thermal Efficiency Model Results

Based on the lower temperature data from Phase 2, the 500°C efficiency test data, and the estimated 700°C efficiency from the transient tests, the DSPHR efficiency has been modeled statistically with the results shown in Figure 13 below, which was presented in the Phase 3 Q5 report. Note that the model efficiency results approach but fall below a reasonable upper limit, defined by high optical efficiency and minimal convective loss. Also note that the model, of course, shows the expected increase with concentration ratio.

Mesh Durability Testing

Two versions of high temperature mesh testing have been accomplished during Phase 3, (1) irradiation in the HFSS and (2) furnace testing. As described above, the solar simulator has been used to test the small scale PHR at an average of at least 1000 suns during the efficiency testing. This testing demonstrated that exposed mesh edges hold up for long enough to reach equilibrium under exposure to irradiation far greater than 1000 suns. For longer duration evaluation, candidate meshes were tested in a lab furnace.

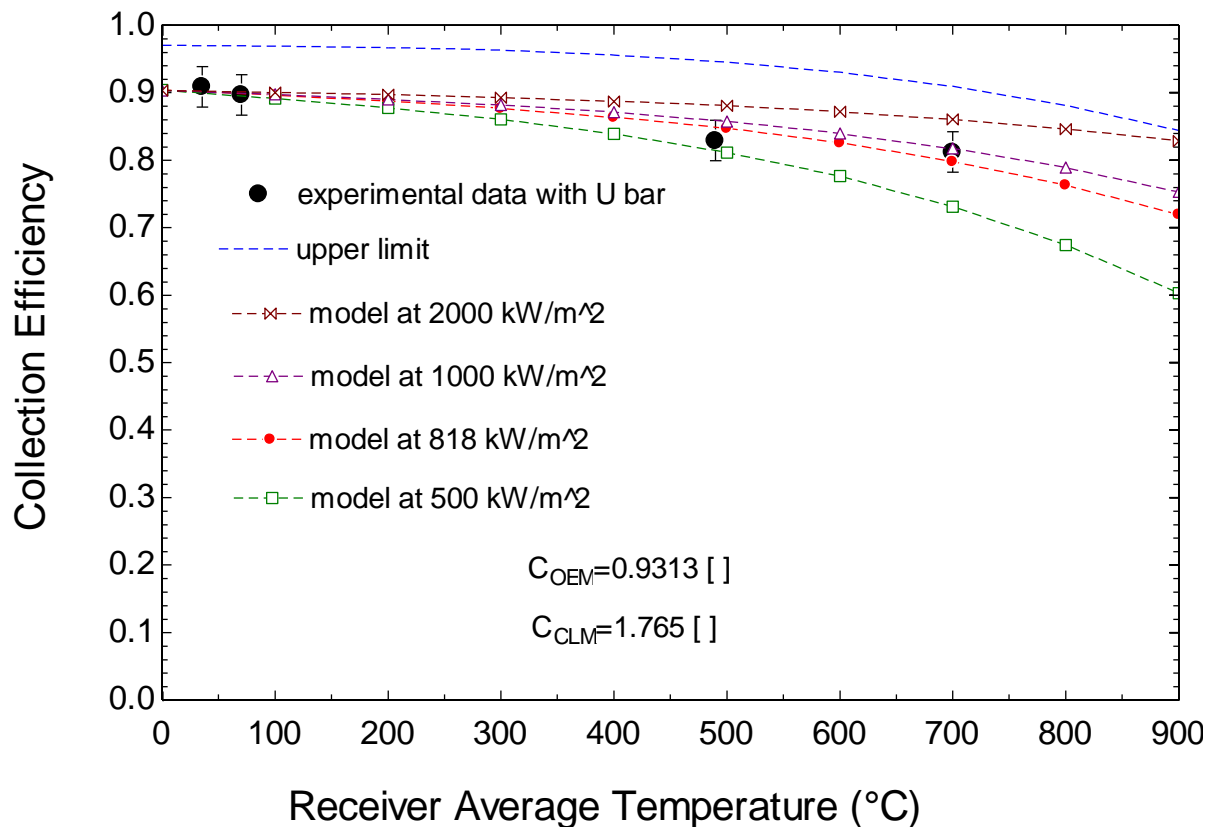


Figure 13. Model compared with experiment for various concentrated flux levels

High Temperature Mesh Tests

The high temperature furnace mesh tests were done in response to the melting of the 316 stainless steel meshes in the initial DSPHR panel at SNL. Details of this testing were presented in the Phase 3 Q5 report and the testing was completed in January 2016. The materials in the furnace test experienced about 10 days at 900°C, 7 days at 1000°C and over 6 days at 1100°C. The resulting oxidation or shedding was observed by mass measuring and calculating the normalized mass and plotting the result with time. Of the tested samples only Monel 400 and Titanium (UNS R50550) obviously experienced extreme oxidation, evidenced both by mass measurement and through visual as well as tactile inspection (Table 5). With these materials removed, Figure 14 shows the changes in mass of the other materials with time. Note that the mass changes in these samples are less than a 0.1% of original mass. It should be noted that a significant different between these isothermal tests and the on-sun tests is that particles were continually flowing over the different mesh materials while heated. Thus, abrasion and wear was more pronounced in the on-sun tests at Sandia. Table 5 and Figure 14 only indicate the potential for corrosion resistance at high isothermal temperatures. As shown in Table 4, although the nickel-based alloys showed a resistance to corrosion relative to the SS316, the high temperatures (possibly non-uniform) combined with particle flow caused additional deterioration that was not evident in the isothermal oven tests.

Table 5: Mesh Types for High Temperature Tests

Material	Monel 400	Inconel 600	Inconel 601	Incoloy 800	Hastelloy C276	Hastelloy X	Kanthal D	Titanium R50550	Stainless 304	Stainless 316
Mesh Count	10x10	10x10	10x10	10x10	10x10	10x10	8x8	10x10	10x10	10x10
Wire Diameter	0.025"	0.025"	0.025"	0.025"	0.025"	0.025"	0.028"	0.025"	0.025"	0.025"
10 Days 900°C	Brittle	Maleable	Stiff Maleable	Maleable	Stiff Maleable	Stiff Maleable	Stiff	Brittle	Maleable	Maleable
7 Days 1000°C	Very Brittle	Maleable	Stiff Maleable	Stiff Maleable	Stiff Maleable	Stiff Maleable	Stiff (Flakes)	Very Brittle	Maleable	Maleable
6 Days 1100°C	Very Brittle	Maleable	Maleable	Stiff Maleable	Stiff Maleable	Stiff Maleable	Stiff (Flakes)	Very Brittle	Maleable (Powder)	Maleable (Powder)
Normalized Oxidation	1.2274	1.0020	1.0020	1.0019	1.0005	1.0016	1.0023	1.2251	0.9960	0.9999

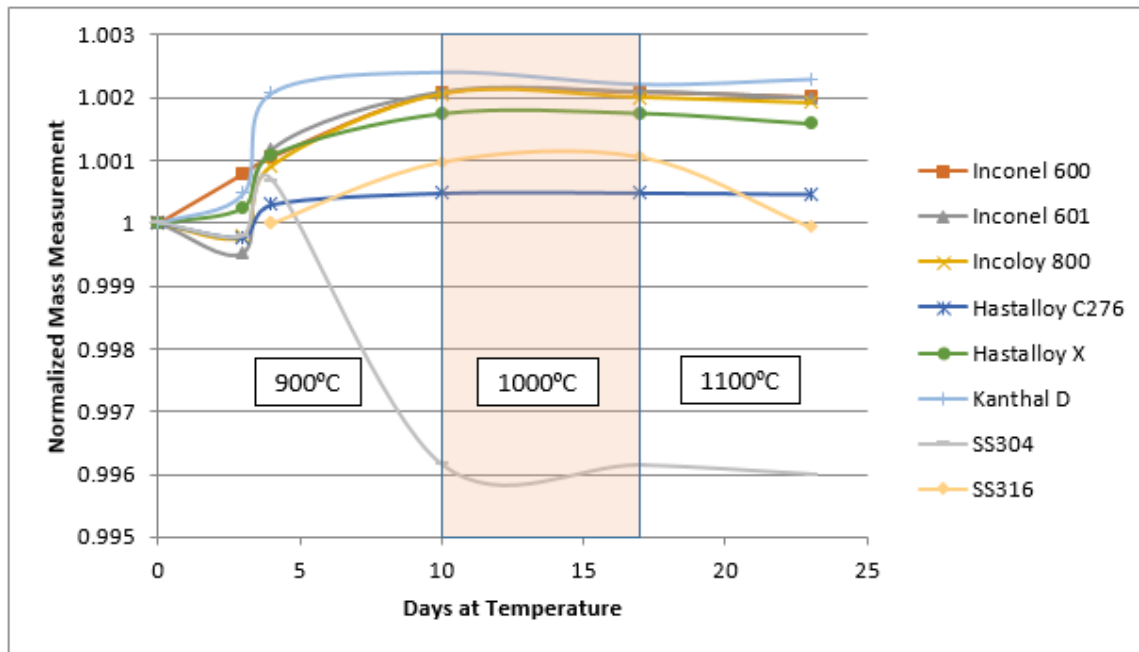


Figure 14: Normalized mass change of preferred high temperature materials

Kanthal D showed highly visual oxidation changes and at the higher temperature flakes would also occur. The stainless steels at the higher temperatures started exhibiting powdery residue. Of the remaining materials, all had been selected for their high temperature performance based on known industrial recommendations and literature. All saw a relatively small initial weight gain followed by fairly constant mass. Of these Inconel 601 and Hastalloy X were supposed to have particularly high oxidation resistance. Hastalloy C276 is similar to Hastalloy X and is reported to have even better corrosion resistance, but it is more expensive. Going forward Inconel 601 and Hastalloy X and Hastalloy C276 were used in the new DSPHR panel, and SS316 was included again to serve as a control. The Hastalloy C276 was used only because it happened to

be available in sufficient amount, since these meshes are only made on demand and are not generally stocked in quantity. These materials are installed in continuous vertical groups of meshes with the Hastalloy X alternating by row in one column of the Hastalloy group in the insert used at Sandia (see *On-sun mesh durability evaluation*, p. 16).

Subsystem 2: Particles

Radiative properties of particles

The overarching goal of Task 2.1 was to identify and develop particle absorber media exhibiting improved solar weighted absorptance and stability in air during extended service at 700°C. All of the unmodified commercially available particle candidate materials (proppants) evaluated in FY13 and FY14 showed some amount of degradation of solar weighted absorptance (Figure 15a) following extended heating in air at 700°C, with the properties of the materials changing most in the infrared region of the spectrum (Figure 15b). The rate of degradation of all particles decreased with time. Both CARBOHSP and ACCUCAST appear to stabilize near $\alpha_s=0.9$ when heated for 500 hours. The decrease in solar absorptance with time is believed to be a result of an oxidation reaction.

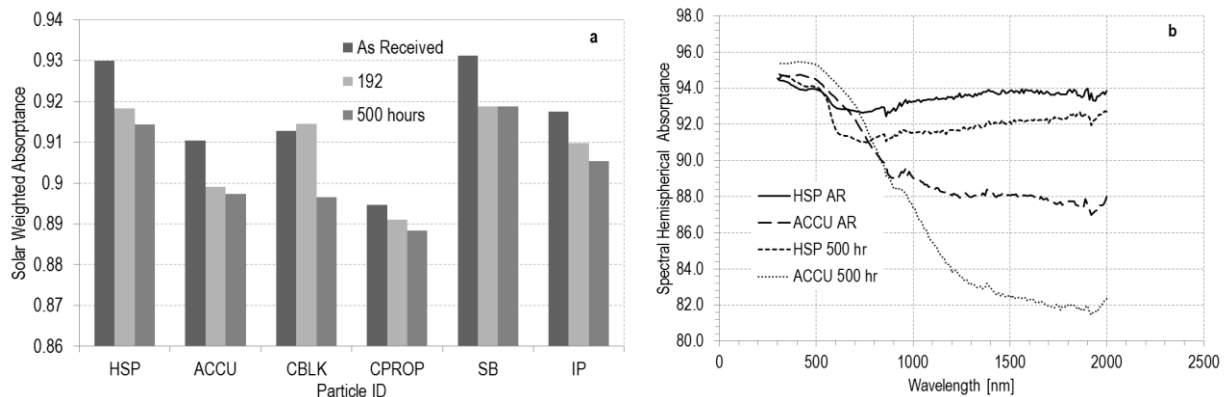


Figure 15. a) The solar weighted absorptance of candidate commercial particles following heating in air at 700 °C and b) The absorptance spectra of CARBOHSP and ACCUCAST in the as received (AR) condition and after heating for 500 hours. The uncertainty of these measured values is +/- 0.3 absorptance units.

Work to develop improved particle absorbers included two technical thrusts. In the first, it was demonstrated that exposing commercially available proppant media to forming gas, a mixture of hydrogen (5%) and nitrogen (95%), improved particle absorptance relative to the as-received condition and, when the reduction was carried out at high temperature, stabilized the solar weighted absorptance of the particles at > 95% following extended exposure to air at 700°C. The second technical thrust focused on the discovery of new absorber materials. In this effort over 140 unique compounds were synthesized and their solar weighted absorptance and thermal emittance evaluated in both the as-received condition and following extended exposure to air at 700°C. Of

these, over twenty were found that maintained a solar weighted absorptance exceeding 85% following exposure. Finally, the work plan for Task 2.1 originally included some effort dedicated to the development of a solar-selective particle, but this work was de-emphasized later in the project following studies showing thermal emittance to be relatively less important than solar weighted absorptance. Despite this change the selectivity of all candidate materials was assessed and two formulations were found that satisfied milestone 2.1.4 (selectivity). Milestone 2.1.3 was satisfied by CARBO HSP reduced in forming gas at 1400°C. Preliminary particle development results were presented at SolarPaces 2013, appearing in the conference proceedings published by Energy Procedia [42]. This work was later expanded with additional characterization data and published as a full length research article in the ASME Journal of Solar Energy Engineering [4].

Work on Task 2.1 was mostly completed at the conclusion of Phase 2 (FY14) following the successful completion of both task milestones; however, during the end-of-phase review it was noted that the solid particle receiver could be used for operation beyond 700°C given a suitable particle. As such, additional work was undertaken to evaluate the stability of our best-performing particle formulation for extended service in air at 800°C. The results of this study are presented below.

Particle Reduction and Thermal Exposure Testing

During Phase 2 of this project we demonstrated that CARBOHSP reduced at 1400°C and heated in air at 700°C maintained a solar weighted absorptance above 95% following 1500 hours of exposure. In addition, the value of solar weighted absorptance did not change across an exposure period ranging from 500 to 1500 hours, indicating that this property was stable. Two questions related to particle properties were raised during the Phase 2 project review:

1. How will the radiative properties respond to heating at 800°C?
2. Can a lower concentration of forming gas be used to chemically reduce the particles?

A series of tests aimed at answering these two questions was completed in Phase 3. The tests include:

1. Synthesis of CARBOHSP reduced at 1400°C with forming gas (5%H₂:95%N₂) and heating of these particles at both 700°C and 800°C for 196, 500, 1000, and 1500 hours.
2. Synthesis of CARBOHSP reduced at 1400°C with forming gas (0.8%H₂:99.2%N₂) and heating of these particles at both 700°C and 800°C for 196, 500, 1000, and 1500 hours. 800°C exposure tests were continued with additional data points at 3900 hours and 4400 hours.

The test results, investigating both 800°C operation and chemical reduction with a lower concentration of forming gas, are summarized in Figure 16.

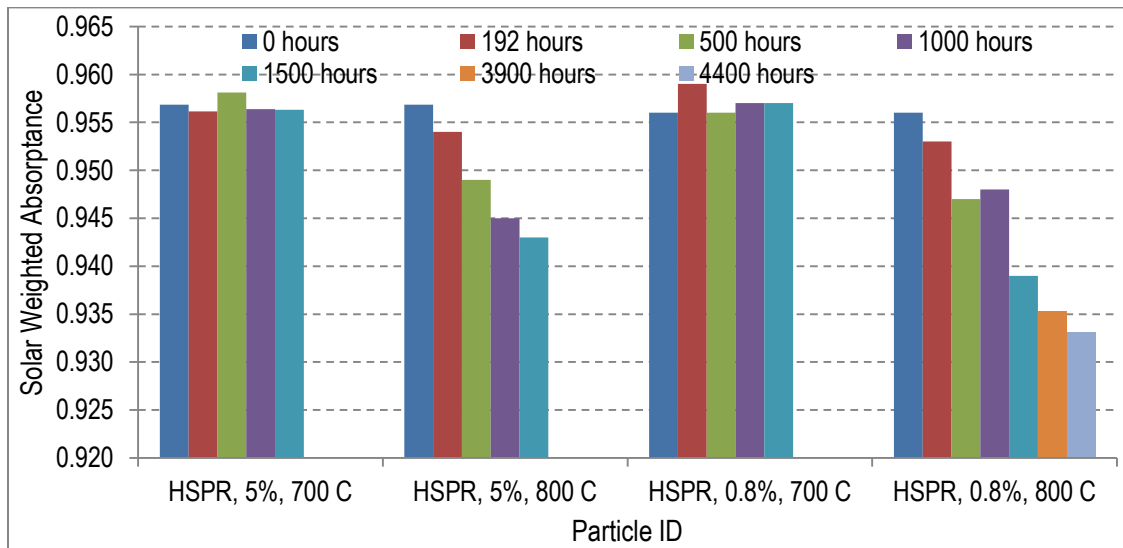


Figure 16. Solar weighted absorptance of reduced CARBO HSP out to 1500 hours of exposure to air at either 700°C or 800°C, with additional data points for HSPR reduced at 0.8% H₂ and exposed at 800°C.

These results show that particles exposed to air at 700°C can be considered stable when reduced in a forming gas concentration above 0.8% H₂ in N₂. The results also show that the solar weighted absorptance is not stable, out to 4400 hours, when the particles are heated to and held at 800°C in air irrespective of the concentration of forming gas used for the reduction. That said, the data points at 1500, 3900, and 4400 hours do indicate that the degradation rate is diminishing with time, leaving open the possibility that HSPR will be suitable for extended operation at 800°C. Figure 17 shows a sequence of images of HSPR following exposure testing and provides a qualitative illustration of the change in optical properties due to extended heating in air. To date, only reduced CARBO HSP has been evaluated at 800°C. Other formulations identified in Phase 2 of this project may be more stable at 800°C, and could also enable operation of the solid particle receiver above 700°C.

It should be noted that the solar absorptance of CARBO ACCUCAST ID50 was measured before and after nearly 200 hours of on-sun testing in the 1 MW_t falling particle receiver prototype, and the measured packed-bed solar absorptance of the used particles (0.946 ± 0.003) was found to be statistically the same as that of the unused particles (0.945 ± 0.001) using a two-sample t-test with a 95% confidence (T statistic = 1.18 using a pooled estimator with 4 degrees of freedom, which was less than the critical t-value of 2.78). The color of the particles was also nearly the same (Figure 18). One theory is that the discoloration to a more reddish brown color is caused by the formation of iron oxide, in particular hematite, which has a reddish brown color. However, as the particles wear and abrade during testing (see next section), especially from the Olds elevator, the hematite is worn off, which would explain the lack of observed particle color change during our on-sun tests (during the isothermal oven tests, no significant abrasion occurred). The middle photo shown in Figure 3 (p. 9) lends credence to this theory since the inside walls of the cavity receiver are now

covered in a layer of reddish-brown/orange dust. It is possible that abraded dust from the particles attached to the hot walls and then oxidized, forming the orange hematite on the walls. The dust from the particles may pose a problem if they soil the heliostats, but significant soiling on our heliostats from the particles was not observed.



Figure 17. CARBOHSP reduced at 1400°C in 5% H_2 :95% N_2 and exposed to air at 800°C for up to 1500 hours



Figure 18. Used (left) and unused (right) CARBO Accucast ID50 particles. Used particles experienced nearly 200 hours of on-sun testing.

Particle Durability

Testing and analysis in Phase 1 showed that the particle attrition rate due to abrasion and wear in a continuously rotating and heated apparatus was less than 0.01% of the particle mass flow rate (typically $1 \times 10^{-5}\%$ – $1 \times 10^{-4}\%$) for various sands and artificial proppants, even at temperatures higher than anticipated in a commercial-scale receiver [36]. As expected, alumina proppants, which are harder and more spherical than common sands, performed better than the sand. All of the candidates exceeded the milestone target attrition rate of 0.01% regardless of size, density, and material for these tests. Furthermore, additional testing in Phase 1 showed that, as reported in [43], particulate stored at the bottom of a tall hot storage bin is not likely to sinter for the purposes of particle storage.

More recently, after nearly 200 hours of on-sun testing with particle temperature periodically exceeding 700 – 800 °C, the particle size distribution and composition of CARBO Accucast ID50 was analyzed using a scanning electron microscope and energy dispersive spectroscopy (SEM/EDS). In the SEM images (Figure 19), it is evident that the used particle sizes are smaller. Particle sizes were measured using the scale in the SEM images to determine the particle size distribution before and after testing (Figure 20). The particle size distribution reported by CARBO Ceramics (accounting for average particle size in between reported mesh sizes) is also shown in Figure 20, and it matches the measured particle size distribution of the unused sample quite well. The average particle diameter of the used particles was found to be ~20% less than that of the unused particles.

Based on the hours of testing and average particle flow rate during the tests (~4.4 kg/s), we estimated that the particle attrition from friction and abrasion was ~0.023% of the particle mass flow rate. The total rate of particle mass loss, including both attrition and loss through the aperture, was estimated by periodically measuring the particle level in the particle collection hopper. The total particle loss was estimated to be 0.06% of the particle mass flow rate, or about 9.4 kg/hr. Of the total particle loss, roughly 3.6 kg/hr (38%) was lost due to attrition, and the balance, 5.8 kg/hr (62%), was attributed to loss due to wind and other convective currents that blew particles out of the receiver through the aperture. The high rate of attrition during the on-sun tests is likely due to the high friction in the Olds elevator, which relies on particle friction with its rotating casing to lift particle up the stationary screw. Larger scale systems would employ skip hoists or other means that have less friction and higher lift efficiencies (see Particle Durability). Particle loss through the aperture can be better controlled through improved geometries or partial coverings over the aperture (see Scale-Up Considerations). During the course of testing, fresh particles were added to the collection hopper twice (11/19/15 and 2/16/16) to replenish the system.

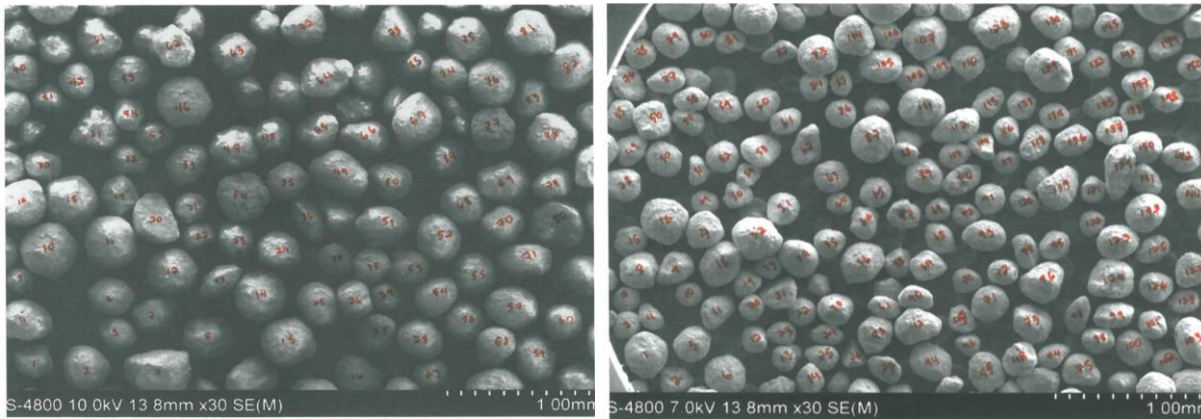


Figure 19. SEM images of ACCUCAST ID50 before (left) and after (right) 187 hours of testing in the on-sun particle receiver prototype. Numbers were added to images for processing particle sizes.

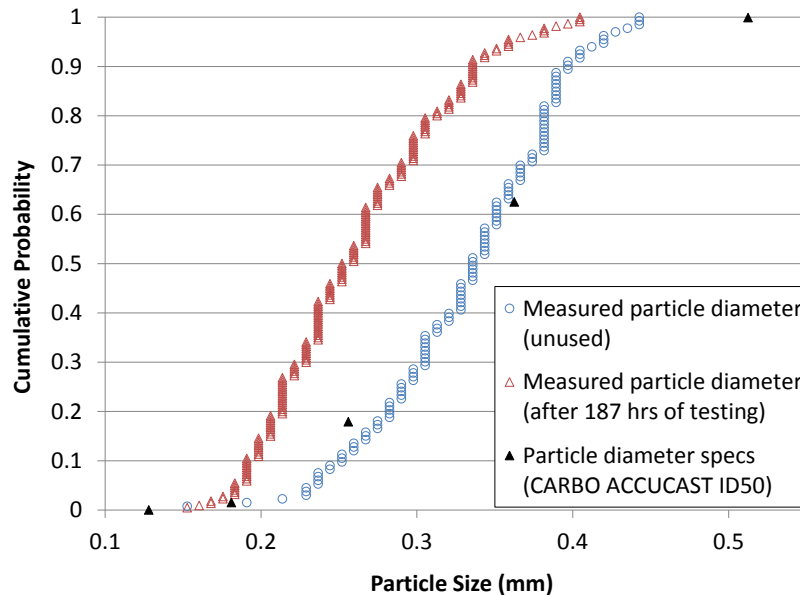


Figure 20. Particle size distribution before and after testing.

The composition of the CARBO Accucast ID50 particles before and after testing is shown in Table 6. The composition after testing appears to shift to somewhat higher concentrations of iron (oxide) relative to the other oxides (alumina, silica), which are the primary constituents of the particles. Two forms of iron oxides are likely to exist: magnetite, which is dark black, and hematite, which can be reddish brown in color. Depending on the phase and composition of the iron oxides, the color and solar absorptance may change. One possibility is that particle abrasion and wear may alter the composition of the original particles, causing a counteracting effect of the oxidation, color change, and reduction in solar absorptance measured in the isothermal oven-based tests and described in the previous section (Figure 17). However, the abrasion

of the particles after testing appears to be fairly uniform as seen in Figure 19 (particles are still spherical). So, a change in particle composition caused by uniform abrasion seems unlikely, unless the composition of the particles is non-uniform, or if the increase in iron oxide is due to a formation of hematite at the surface, which can be worn away. Future studies should try to examine the spatial composition of the particles and determine if wear has any impact on the optical properties.

Table 6. Composition of particles before and after testing identified through EDS.

Element	Unused CARBO ACCUCAST ID50 (wt%)	Used CARBO ACCUCAST ID50 (after 187 hrs of testing) (wt%)
O	45 - 46	46 - 47
Al	38 - 39	37 - 38
Si	8.9 - 9.6	6.5 - 8.8
Ti	1.3 - 1.4	1.2 - 1.3
Fe	5.2 - 5.4	6.7 - 7.9

Subsystem 3: Balance of Plant

Thermal Storage

Work on the thermal energy storage (TES) subsystem started with the identification of a suitable thermal energy storage (TES) bin design. A three-stage approach was devised for this purpose. The first stage was the identification of all potential design concepts and preliminary selection of preferred concepts. Table 7 summarizes all the TES design concepts that were considered, along with the team's qualitative assessment of their feasibility:

Table 7. List of TES design concepts

Design Basis	Design Code	Advantages	Disadvantages	Assessment
Structural	S1: Steel or metal frame	Relatively inexpensive	<ul style="list-style-type: none"> Common metallic materials soften at target temperatures Thermal expansion can cause adverse cycling effects 	Not suitable – Does not meet high-temperature requirements of Milestone 3.1.1
	S2: Exotic metal frame	Withstands high-temperatures	<ul style="list-style-type: none"> Expensive Thermal expansion an issue 	Not suitable – Does not help meet cost targets
	S3: Layers of firebrick + reinforced concrete	<ul style="list-style-type: none"> Common and inexpensive Structurally sound 	Poor insulation	Not suitable – Not expected to meet heat loss limit of Milestone 3.1.1

Design Basis	Design Code	Advantages	Disadvantages	Assessment
	S4: Layers of insulating firebrick + reinforced concrete	High thermal insulation	<ul style="list-style-type: none"> Strength can be an issue Using insulating firebrick alone for insulation is costly 	Not suitable – Strength is questionable; does not help meet cost targets
	S5: Layers of firebrick + insulating concrete + reinforced concrete	<ul style="list-style-type: none"> Common and inexpensive Acceptable strength 	Insulation acceptable but not optimal	Warrants further investigation
	S6: Layers of insulating firebrick + insulating concrete + reinforced concrete	<ul style="list-style-type: none"> Common Acceptable strength Superior insulation 	Relatively higher cost than S5.	Warrants further investigation
Geometry	G1: Rectangular shaped bin	Easy to construct, instrument and test	Corners may suffer excessive stresses	Warrants further investigation
	G2: Round shaped bin	More care needed in construction	High structural integrity	Warrants further investigation

Based on the table above, Structural Designs S5 and S6, and Geometric Designs G1 and G2 were shortlisted for further investigation. The second stage was the study of potential materials of construction for the preferred concepts. The materials considered for Structural Designs S5 and S6 were firebrick (FB), insulating firebrick (IFB), autoclaved aerated concrete (AAC), perlite concrete (PC), perlite-refractory concrete (PRC), expansion joint (EJ) and reinforced concrete (RC). The expansion joint was necessary to allow the expansion between the outer layer of reinforced concrete and the next internal layer.

The third stage was to test and simulate prototype TES bin designs for the preferred concepts. A TES bin with Structural Design S6 and Geometric Design G1 was constructed. In this design, the wall was made of a 4"-insulating firebrick (IFB) layer, a 16"-perlite concrete (PC) layer, a 0.5"-expansion joint (EJ) layer, and an 8"-reinforced concrete (RC) layer. However, this was done on only one half of the walls. In the other half, only PC was used to test the durability of PC directly exposed to extreme temperatures. Also, a large LPG tank was installed on site to ensure stable supply of fuel to the bin. No inlet or outlet portals were included in the bin. The experiment was continuously run for nearly 45 hours, during which the temperature was maintained at about 800°C, and steady state conditions were closely approximated. It was found that the steady state heat loss was approximately 4.4%. This calculation was based on measurements of the temperature difference across the expansion joint and its known thickness and thermal conductivity. Using dimensional analysis, this value was shown to correspond to a heat loss of less than 1% per day from a large-scale TES bin. Furthermore, inspection of the materials used to construct the TES system showed that they remained intact and did not show any appreciable signs of cracking or wearing.

Despite the fact that the above design achieved Milestone 3.1.1, the project team preferred a TES bin with Structural Design S6 and Geometric Design G2. This design

was structurally more robust and it was more representative of the TES bins that would be built in large scale plants. Furthermore, more prototypical design features were built into this design. For example, the middle section of the wall was made of perlite concrete in which refractory cement was used instead of Portland cement for even higher temperature resistance. This design was chosen to be built within the Riyadh Techno Valley (RTV) tower facility.

To help inform the design process of this TES bin, a ground-based mock-up was built. In this bin, heating of the internal cavity was done using an electric heater instead of an LPG burner for better temperature control. The dimensions of this TES bin closely matched those of the upper part of the RTV TES bin, and the wall construction was also identical to the proposed RTV TES bin. Figure 21 shows a photograph of this TES bin.



Figure 21. Ground-based cylindrical TES test facility, (a) overall view of the cylindrical TES bin, (b) the electric heater inserted along the centerline of the TES bin.

Despite the usefulness of the ground-based cylindrical TES bin in informing the design process of the RTV bin, especially to obtain accurate data about thermal conductivity of various layers (as will be shown later), the ground-based bin could not be used to understand the transient heat loss effects. In the ground-based TES bin, LPG was used to simulate the presence of hot particles that filled the entire bin. To study the transient heat loss effects, we needed to simulate a partially filled bin, and we needed to be able to vary the level with which the bins were filled. This could not be represented with LPG burners or electric heaters. Furthermore, the RTV facility was not completed at that time. Therefore, it was necessary to revert to numerical modeling of the transient heat loss in the RTV bin.

The TES bin in the RTV tower is “sandwiched” between the receiver cavity on the top and the particle-to-working-fluid heat exchanger (PWFHX) on the bottom. The reduced dimensions of the bin at the bottom were due to the smaller size of the already built PWFHX. This transition was made possible by having additional layers of insulating firebrick extending further into the TES bin, meaning that the bottom half will be more thermally insulated than the top half.

Under normal operation, the TES bin would receive particles from the top for approximately 7 hours (the nominal daytime operating period of the facility). Some of the particles admitted to the TES bin would be forwarded to the PWFHX beneath, while the remaining particles slowly accumulate and eventually fill the TES bin. Once the daytime operation ends, the full TES bin starts depleting its particle inventory such that the PWFHX continues to operate for an additional 5.25 hours. This means that the RTV TES bin has a storage capacity of 5.25 hours. This duration was governed by a number of engineering constraints unique to this facility. Studying energy loss from a TES bin with the above mentioned geometry and operational constraints was complex, hence the need for numerical modeling. A model was built to simulate the full charge-discharge process over multiple cycles. Due to the transient nature of the problem, it was best to characterize the energy loss by the difference between the energy content of the particles entering the TES bin during the charging process and the energy content of the particles leaving the bin throughout the charging and discharging phases. The numerical simulation was performed using ANSYS FLUENT. In order to shorten the computational time, the Volume-of-Fluid (VOF) approach was used instead of the Eulerian multiphase model. By using VOF model, flows of two or more immiscible fluids can be simulated. Furthermore, VOF model is suitable for flows where the interface is sharp, such as slug, stratified or free-surface flows.

Figure 22 shows the change in average exit temperature during the first and second days of operation. The particles quickly approach the 700-C threshold during the charging period. The temperature remains nearly constant about 4 hours into the discharging period and starts to drop afterwards. The temperature profile for the second day differs significantly during the first 7 hours due to the fact that a more realistic initial temperature is used in the beginning of the second day simulation. It is important to note that the second day simulation also assumed that Boundary A is sealed, with only one tenth of the previous amount of air leakage allowed into the bin. This modification was due to the observation that air leakage into the TES bin after the end of daytime operation on the first day gave rise to vigorous natural convection currents which contributed significantly to energy loss.

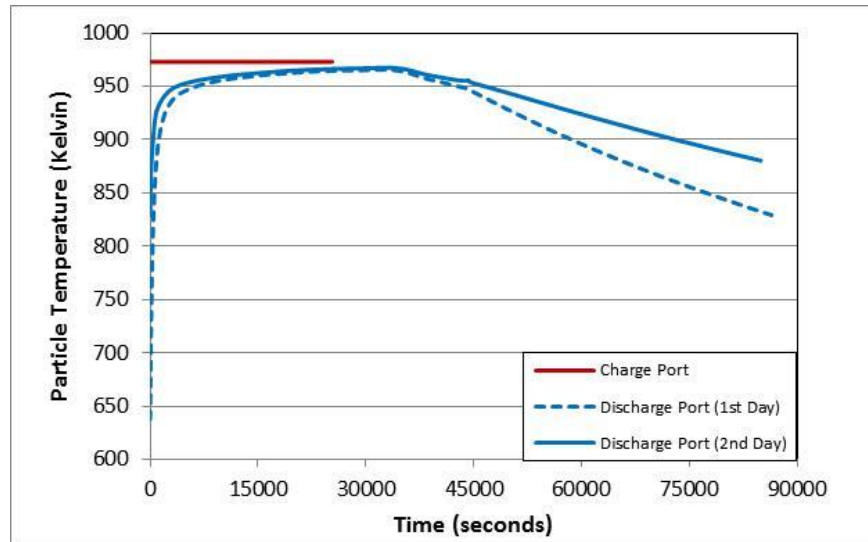


Figure 22. Comparison of average exit temperature for the full 24-hour cycle of the first and second days.

From the above results, the total energy loss for the second day was calculated. It was found that the total energy entering with the particles during daytime operation was 8.32 GJ, whereas the total energy leaving with the particles throughout the charging and discharging periods was 8.04 GJ. This means that the total energy loss is 0.28 GJ, which represents an energy loss of 3.3%. This calculation is based on the reference temperature being the minimum particle temperature in the cycle, i.e. 300°C. This value meets Milestone 3.1.2, which requires energy loss to be less than 4%/day.

While performing the above-mentioned numerical modeling, two other activities were carried out; namely, cost analysis and measurement of thermal conductivity of various layers of the ground-based TES bin mock-up. Table 8 shows the costs involved in building the RTV TES bin.

Table 8. Cost breakdown of the RTV TES bin.

Cost Item	Cost (in US Dollars)	Cost (\$/kWh _{th})
Reinforced concrete (including plywood for forming)	4,900	4.8
Perlite concrete	4,900	4.8
Insulating firebrick	8,700	8.6
Miscellaneous items	2,900	2.8
CARBO Accucast ID50K (7.8 tons to fill TES bin)	12,900	12.7
TOTAL COST	34,300	33.7

The costs in Table 8 were based on a labor rate of approximately \$13.5/hour, which was the actual labor cost incurred during the construction of the TES bin. This rate fell within the range of wages of construction workers provided by the Bureau of Labor

Statistics. The cost of the particles was based on a quotation SNL received from CARBO, which indicated that the cost of Accucast ID50K in the 10,000 lb to 40,000 lb range would be approximately \$0.75/lb. The energy content in the particles was calculated to be 3.67 GJ, or 1020 kWh. Therefore, the total cost for this small-sized bin was \$33.7/kWh(th). This cost can be broken down to \$21/kWh(th) for the physical bin and \$12.7/kWh(th) for the particles.

To calculate the cost of a commercial-scale TES bin, the surface-to-volume ratio was assumed to be about 8 times smaller than the RTV TES bin. In this case, the cost of the physical bin would drop from \$21/kWh(th) to \$2.6/kWh(th) due to the reduction in the surface-to-volume ratio. On the other hand the cost of particles would also drop from \$0.75/lb to about \$0.65/lb, since the quantity is larger than 40,000 lb (as per the quote SNL received). This means that the cost of the particles would drop from \$12.7/kWh(th) to \$11/kWh(th). The combined cost would then be \$13.6/kWh(th). This cost met Milestone 3.1.2. Furthermore, the above calculations did not take into account the significant reduction in the cost of building a commercial scale TES bin due to wholesale purchase of materials, mechanized mixing and casting of concrete, and optimized labor sourcing. All the cost estimates constitute a worst-case scenario, i.e. the costs represent an upper limit.²

As mentioned above, the ground-based TES bin was also used to measure thermal conductivity of different layers. The resulting data would serve as a valuable resource for future modeling of these systems. For this purpose, the ground-based TES bin was instrumented with an electric heater that can supply as much as 30 kW, where the level of heating can be controlled externally. Temperature measurements were taken by 55 thermocouples. These thermocouples were inserted between all wall interfaces, and they are distributed circumferentially and axially. Three power levels were tested. Those levels correspond to inner temperatures within the TES bin of 300°C, 500°C, and 700°C. Three runs were performed at each of the three temperature levels. It is important to note that the daily variation in ambient temperature made it impractical to estimate the thermal conductivity of reinforced concrete using this setup. For this reason, a numerical model was built using the same rebar spacing and well documented information about the thermal conductivities of steel rebar and concrete aggregate. Table 9 summarizes the results of this test campaign

Table 9. Values of thermal conductivity and standard deviation of TES bin layers

Temp. setting	Insulating firebrick, FB			Perlite concrete, PC			Expansion joint, EJ		
	Temp. [°C]	k [W/m.°C]	Standard deviation of the means [%]	Temp. [°C]	k [W/m.°C]	Standard deviation of the means [%]	Temp. [°C]	k [W/m.°C]	Standard deviation of the means [%]
300 °C	268.30	0.218400	2.6	161.90	0.112500	2.4	60.94	0.045510	1.5
500 °C	438.20	0.168900	2.3	244.60	0.113700	2.2	70.08	0.046590	1.5
700 °C	640.90	0.225700	2.2	362.70	0.145500	2.1	104.70	0.051360	1.5

² All the figures used in estimating material costs were based on local procurement costs in Saudi Arabia, which are significantly higher than the costs in the U.S. (except for Portland cement used in the outer reinforced concrete layer).

In the mean time, numerical simulation showed that the effective thermal conductivity of the reinforced concrete had minimal variation with temperature. The average effective thermal conductivity was found to be 1.91 W/m.K

The final subtask was to conduct an on-sun test of the RTV TES bin with inlet and outlet ports in mind. This subtask has been severely delayed due to multiple delays and stoppages of site work during the construction project. The RTV facility is now ready for testing. Figure 23 shows a live test during commissioning of the facility.



Figure 23. Live test of the completed RTV facility

Figure 24 shows the cover that was installed on the top of the TES bin to serve as an inlet port. The outlet port is naturally the interface between the TES bin and the heat exchanger beneath it.

The test procedure is straightforward. Red sand is circulated through the system to be preheated. Once the thermocouples at the outlet of the TES bin indicate that the target temperature has been reached, readings of temperature from the thermocouples installed within each layer will be used to estimate heat loss.

To partially meet Milestone 3.1.2, calculations were made using the experimental data obtained from the ground-based TES bin, and those calculations showed that the heat loss would be 4.88% per day. These calculations do not consider the presence of particles inside the bin. The presence of particles increases thermal resistance due to the particles' low thermal conductivity. This means that the value of 4.88% constitutes an upper limit to heat loss.



Figure 24. (a) Top of the TES bin, (b) Top cover of the TES bin

Heat Exchanger

In Phase 1, lab-scale heat-transfer experiments were conducted showing heat transfer coefficients around $100 \text{ W/m}^2\text{-K}$ for conditions expected in the particle-to-working-fluid-heat-exchanger (PWFHX) and reported in [35, 39]. Furthermore, an intermediate scale experimental (ISE) exchanger (overall volume around 1.0 ft^3) was built and tested [44]. The aim was to validate in practice the heat transfer coefficient model developed based on the small bench-top experiment. The results obtained using the ISE HXer show heat transfer coefficients above $100 \text{ W/m}^2\text{-K}$ confirming our lab model and even indicating that our lab results are somewhat conservative. Knowledge from these physical and practical experiments was especially helpful in guiding the subsequent design work.

Milestone 3.2.1 in Phase 1 requires a preliminary PWFHX with 90% exergetic efficiency and a commercialized PWFHX with 95% exergetic efficiency. In this task, a 6 MW-th prototype-scale exchanger was designed for operation at maximum temperature of 700 C and exergetic efficiency of 90%, with estimated technologically-mature cost approximately 25 \$/kW. A similar but larger and more advanced 60 MW-th exchanger was also designed for operation at maximum temperature of 800 C and exergetic efficiency of 95% and is also projected to cost around 25 \$/kW. Standard heat transfer models and specific experimental results along with standard cost-engineering methods have been used to develop these designs and cost estimates. Consequently, this task has successfully met the criteria in Milestone 3.2.1 during Phase 1.

In Phase 2, four alternative particle-fluid heat exchanger (PFHX) designs were developed, assessed, and ranked. The candidate designs that were considered reasonable alternatives are: (1) a serpentine finned-tube (SFT) design with plug flow on the particulate side, (2) a fluidized bed (FB) PFHX, (3) a design with thin or trickling particulate flow (with a free surface) called the zig-zag (ZZ) PFHX, and (4) a parallel pillow-plate (PP) PFHX also with plug flow. Subsequently, finned tubing in the FB-FT-HX is also under consideration. The four general design concepts are illustrated in Figure 25.

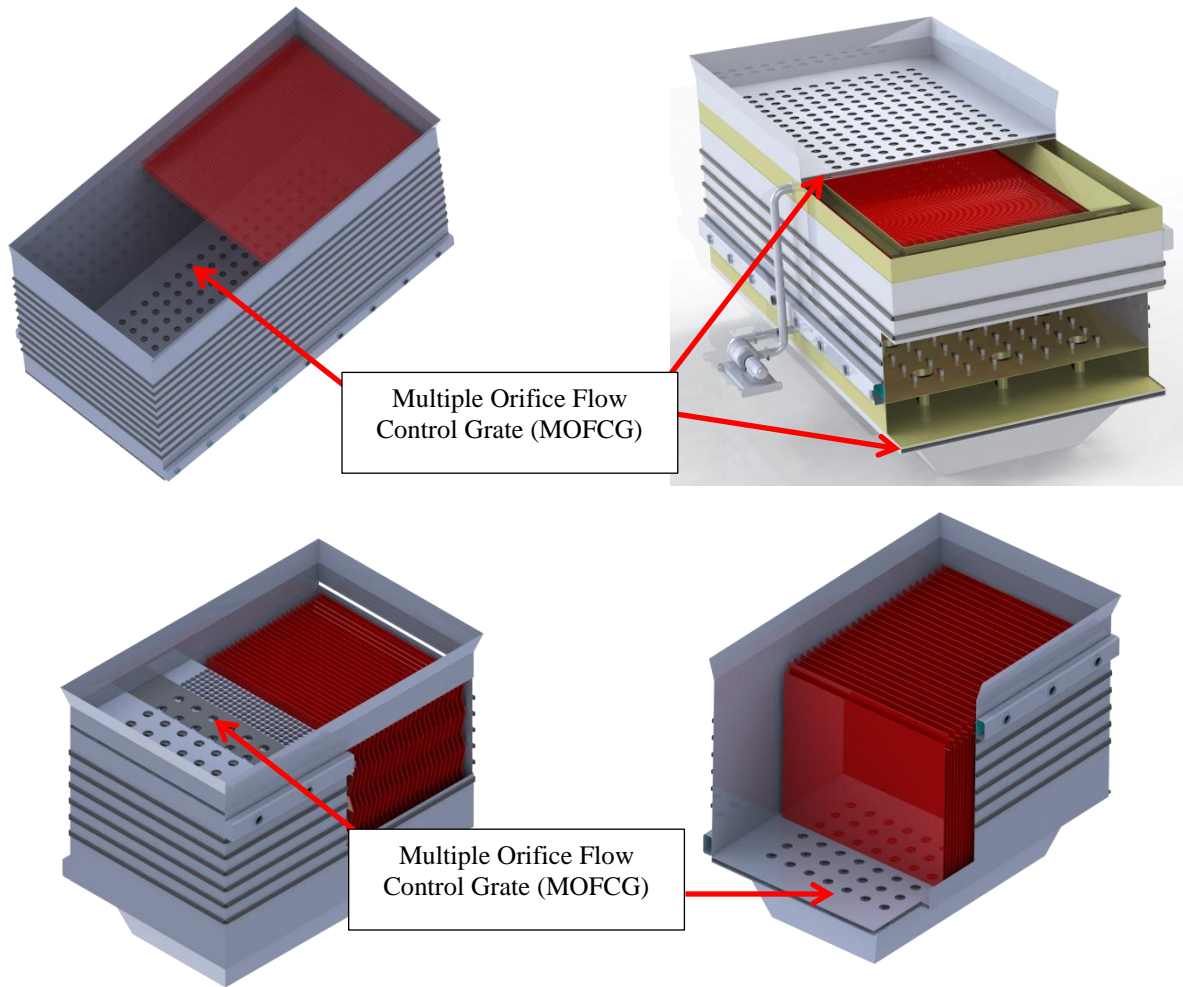


Figure 25. Top Left: Serpentine Finned Tube (SFT) HX (most tubes omitted for clarity; Top Right: Fluidized Bed (FB) PFHX; Bottom Left: Zig-Zag (ZZ) free-surface flow HX (corrugations in the plates are exaggerated for clarity); Bottom Right: Parallel Pillow Plate (PP) HX (in section showing plates and multiple orifice flow control grate (MOFCG)).

The HX design and cost models were developed and presented in Phase 2. At the completion of optimization and design integration, the results shown in Table 10 were generated. This task required HTF and cost models to compare the candidates. Any acceptable HX design must balance the pressure losses in the media with the equipment cost. Otherwise, capital cost erroneously reduced by enhancing the heat transfer coefficient (HTC) without penalty for pressure loss (or fluidization) result in a non-economical design. We address this issue by optimizing the HX design to minimize the life cycle cost (LCC) by adding to the equipment cost the LCC of pumping on the working fluid (e.g., s-CO₂) and the cost of fluidization, if applicable. The LCC requires an economic scenario, so we have chosen a typical 30 year life and 3% MARR resulting in 19.6 as the LCC factor. This approach yields a minimum LCC design balancing equipment and operating cost. Note that the LCC is a design tool dependent on a reasonable economic scenario and is distinct from the equipment cost required for

actual construction. Ultimately, this effort has three designs that meet and one that closely approaches the criteria of a projected \$30/kWth installed equipment cost for mature large production design (see Table 10). The cost metric was especially challenging because the design must also achieve a 650 °C outlet temperature requiring a 50°C approach to the 700 °C inlet particulate temperature. The resulting conditions for the 200 bar s-CO₂ are 250 °C inlet and 650 °C outlet, which is consistent with the 400 K temperature rise adopted for this project.

Table 10. Summary of heat exchanger costs and risks for minimum life cycle cost (LCC)

Type	h_{sand} W/m ² -K	Tube mat	Equipment Cost \$/kWth	LCC \$/kWth	P-Risk	I-Risk	SF-Risk
FB-FT	450	CS/SS	16	33	MOD	MOD	LOW
FB*	600	CS/SS	23	39	HIGH	MOD	LOW
FB**	450	CS/SS	26	46	LOW	MOD	LOW
SFT	101	CS/SS	31	36	MOD	MOD	LOW
ZZHX	400	SS	56	N/A***	HIGH	MOD	MOD
PPHX	100	SS	82	N/A***	LOW	LOW	MOD

FB = fluidized bed exchanger, FB-FT = fluidized bed exchanger with finned tubes, SFT = serpentine finned tube, ZZ = zig-zag, PP = pillow plate, HX = heat exchanger.

Tube Materials: SS means stainless 309 or 316 as appropriate; CS/SS designates for tubular designs a combination of carbon steel (CS) in low temperature section and for fins with SS used in high temperature sections as feasible and appropriate..

*higher h_{sand} , near max; **conservative h_{sand} ;

***equipment cost too high – LCC not calculated

P-Risk: performance risk, I-Risk: system integration risk, SF: structural failure risk

Further literature review reveals some research interest in FB HX with finned tubes, both helical and longitudinal fins seem promising; however, we find little commercial or patent literature indicating current industrial interest – probably due to a lack of obvious applications. Nevertheless by applying the existing bare tube mode directly to finned tubes as an expedient approach, we show a large increase in performance and excellent overall economics.

Notably, all the designs feature a simple flow control device we call the Multiple Orifice Flow Control Grate (MOFCG) comprising a moving multiple orifice grate plate sandwiched between support plates and graphite layers serving as gasket and lubricant. It appears that a functionally similar control device may be commercially available; however, the patent implications of our design are still being investigated.

Using the open literature and some vendor data, we have further developed a generic cost model. Various sources for cost data are used and are implemented in a single model, it is straightforward to use the cost results to support optimal design studies.

Four heat exchanger technologies are ranked by optimized LCC in Table 10. We also assess performance risk, system integration risk, and structural failure risk. The fluidized bed design with finned tubes seems most attractive; however a tube based variant of the PPHX (essentially a bare tube version of the SFT) might be considered for the prototype at SNL since tubes replacing plates minimizes the SF-Risk, and construction by an experienced fabricator minimizes the performance and integration risk. Any HX will be costly at small scale, so the projected \$/MWth is less relevant for any proposed prototype.

Particle Lift

Tower Particle Lift

In Phase 1, the design selection and conceptual design and engineering of a commercial scale particle lift system, including the completion of a small-scale model of the proposed design, was completed. Conceptual design drawings and energy efficiency and heat loss modeling were also completed. Detailed efficiency modeling based on reliable published component efficiencies resulted in projected energy efficiency of 80% which exceeds the 75% energy efficiency metric. With this efficiency, the parasitic power should be less than 1% of the rated output. Figure 26 is similar to the so-called Kimberly skip sometimes mentioned in the mining literature. Two conference papers were presented, one described the conceptual design selection process [45], and the other describes the technical analysis [46] used to estimate cost and efficiency and support the concept section.

The selected Kimberly skip is highly adaptable to this application. As seen in Figure 26, this skip is both filled and discharged from the top and has no complicated and leak-prone bottom hatch. This arrangement facilitates a design that is very simple structurally and mechanically. The single top hatch, which is opened and closed by motion of the skip thereby eliminating any mechanical or hydraulic actuators, is critical to this simplicity. Importantly, this design appears to be almost leak proof and should easily achieve much less than 0.1% temporary spillage of particulate during filling and discharge. All such spillage will be accumulated in a sump built into the lift shaft, which can be emptied as necessary; therefore, there will essentially zero net loss of particulate from the system. Minimal heat leak is also an objective, and simplicity of the proposed skip design makes it easy and inexpensive to install adequate internal insulation to keep the heat leak from the skip well under 0.1% of the rated capacity of the system. Our design also envisions an elevator shaft allowed to stay at 200 °C, which further minimizes incidental heat leaks. Altogether the proposed design ensures a minimal heat leak that will have negligible effect on the overall system efficiency.

As reported in Phase 2, the next stage or preliminary design is complete and a refereed paper has been completed and accepted [47] describing the more complete preliminary design. For this paper, special emphasis was placed on developing a more systematic design-specific cost estimate to compare with the vendor estimate and the cost estimates from a generic construction data base. Two small scale models were built during this phase, and our experience with the two small-scale models was convincing with regard to these issues.

Outside review of the design was required and has been obtained. One company familiar with steel fabrication and industrial lift manufacture was first consulted. This company has commented that our design will be easy to manufacture and install. After incorporating some minor modifications based on this review, we consulted with a major skip-hoist component supplier concerning component selection. With helpful input from these initial reviews from smaller companies, we contacted one of the major skip hoist manufacturers. Their review was also favorable, although they have some suggestions that we are now considering.

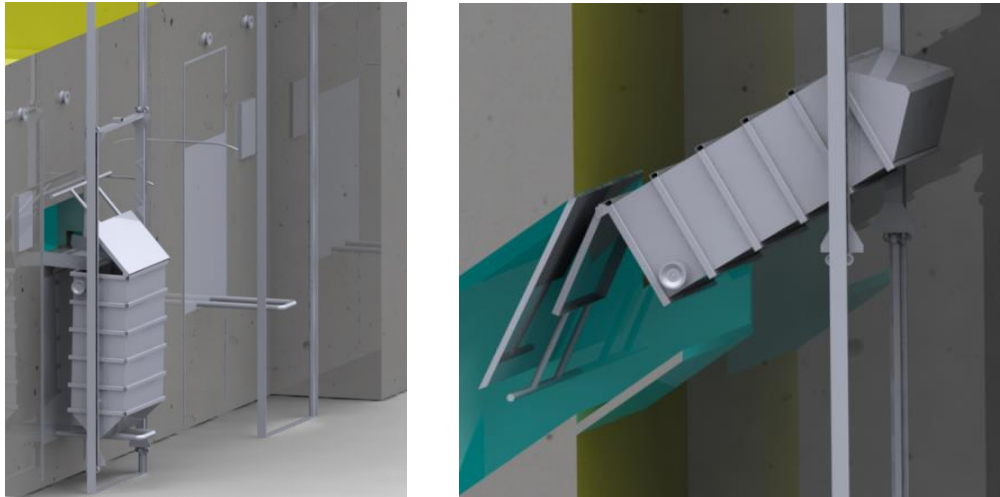


Figure 26. Insulated Kimberly skip charging (left) and discharging (right).

As shown in Figure 27, the Kimberly Skip is easy to integrate into the CSP system. Note that the lift shaft will be kept at elevated temperature around 200 C to minimize heat losses, but the electrical and mechanical equipment (other than the lift drum) will be kept at near ambient temperature for efficiency and economy.

Table 11. Current Cost Analysis for Cold Temperature Particle Lift

Estimated Cost of 2 Skips without Hoist System	\$198,000
Estimated Cost of Hoist System	\$295,000
OLDS Elevator Particulate Recovery system	\$30,000
Total Estimated Cost per System	\$523,000
Total Estimated Particle Lift cost per MWth	\$8,719

Accordingly, the lift system is expected to cost around \$8,719 per MWth, which agrees with previous independent cost estimates using technology-specific cost engineering research results, which was around \$9,614 per MWth.

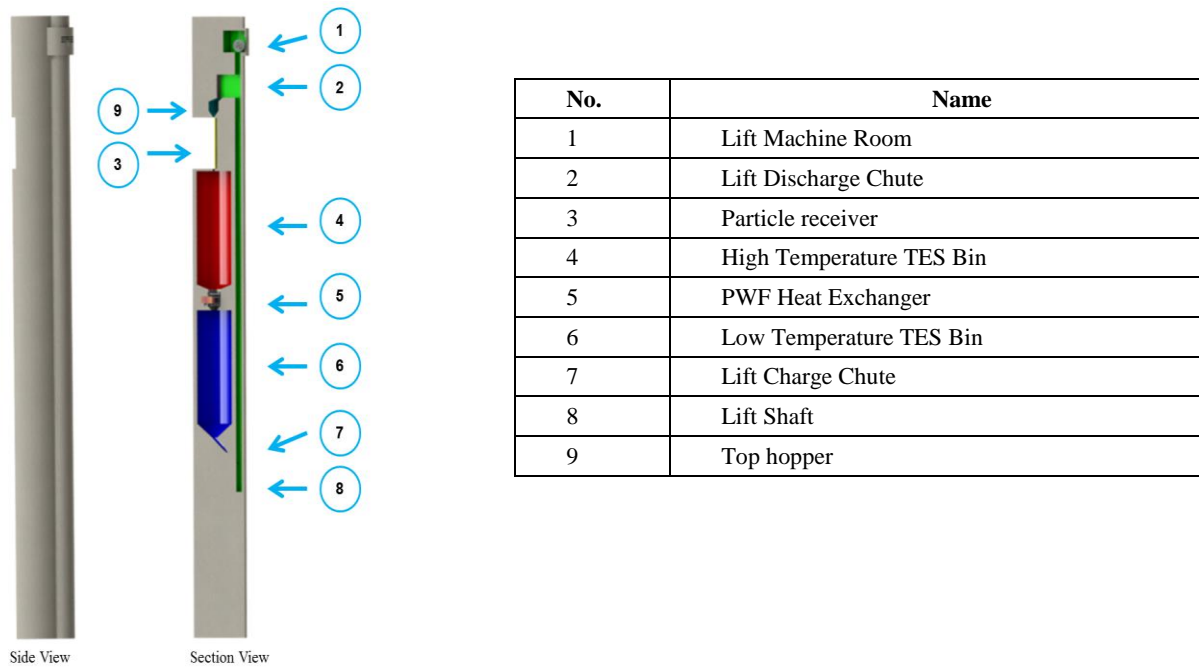


Figure 27. Lift integrated into TES tower showing important components and locations.

Discussion and Path Forward

Cost and performance comparisons

Table 12 presents a comparison of cost and performance metrics for solar thermal receiver technologies. The falling particle receiver technology is one of the few receiver technologies that can provide direct, long-term energy storage. Steam, liquid-sodium, and volumetric-air receivers cannot provide long-term storage due to high pressures or low energy densities of the media. While molten salt can also be heated to provide long-term storage, molten nitrate salts decompose when temperatures reach $\sim 600^\circ\text{C}$ [48]. This prohibits the ability to use higher-temperature and more efficient power cycles. Another disadvantage of molten salts is that they freeze at $\sim 200^\circ\text{C}$. Thus, expensive trace heating is required on all piping and vessels containing the molten salt to ensure that it does not freeze and clog the system.

Another advantage of the particle receiver is that very high solar fluxes (irradiances) can be directly applied to the particles. A high solar irradiance minimizes heat losses relative to the incident power. Because the particles are heated directly, irradiances over $2,000\text{ kW/m}^2$ can be applied. Receivers that utilize fluid flowing through tubes (steam, molten-salt, air receivers) incur additional heat-transfer resistance across the tube walls and from the walls to the fluid, which limits the maximum irradiance to less than 1000 kW/m^2 to keep the temperature of the tube materials below its softening point. Liquid sodium has a very high thermal conductivity, which enables higher irradiances and receiver efficiencies, but sodium reacts violently with water and is flammable in air. The recent

tests have shown that the thermal efficiency of particle receivers can achieve 70 - 80% for small-scale (~1 MW) systems with up to 1000 kW/m² of irradiance. Higher efficiencies (>90%) are expected for large-scale systems approaching 100 MW with higher irradiances [1, 3].

The cost of particle receivers has been estimated to be ~\$125/kW_t, including the cost of the receiver, tower, particle lifts, support structure, insulation, piping, and hoppers [49]. This is less than costs associated with steam, molten-salt, and liquid-sodium receivers. With regard to energy storage, thermal storage using particles yields the lowest cost by over an order of magnitude relative to other large-scale energy-storage technologies such as batteries, pumped hydro, compressed air, and flywheels. Table 13 shows that the levelized cost of thermal storage using particles or molten salt is on the order of ~\$10/MWh_e, whereas the levelized cost of the other technologies ranges from ~\$100/MWh_e to \$1,000/MWh_e. The roundtrip efficiency of thermal storage is also significantly higher (>98%) than that of batteries (60 to 90%, pumped hydro (65 to 80%), compressed air (40 to 70%), or flywheel storage (80 to 90%), which only provides short-term storage on the order of seconds to minutes. Environmental concerns also exist with batteries (heavy metals pose environmental and health concerns) and pumped hydro (water evaporation/consumption). Pumped hydro and compressed air energy storage also require unique resource and geographic requirements, which limits the application of those storage technologies. A significant advantage of particles over molten salt is that the particles can be heated to much higher temperatures (>1,000 °C), which increases the energy storage density and can reduce the cost of thermal storage.

Scale-Up Considerations

In order to scale-up the particle receiver from the 1 MW_t prototype demonstration to larger (≥ 10 MW_e) systems, several additional tests and challenges should be considered:

- Integration with a particle-to-working-fluid heat exchanger, potentially operating at high working-fluid temperatures (700°C) and pressures (20 MPa)
 - We are designing a particle-to-sCO₂ heat exchanger as part of a new (FY16 – FY18) SuNLaMP project that will be demonstrated with the prototype falling particle receiver system.
- Increasing receiver thermal efficiency through consideration of alternative geometries, sizes, aperture nod, multi-stage particle collection and release, and/or segmented quartz tubes to partially cover the aperture
 - Christian et al. [3] showed that a large cavity with a downward facing nod angle yielded the best thermal efficiencies. DLR demonstrated the use of segmented quartz tubes to cover the aperture of a cavity receiver to increase thermal efficiency [50]. The tubes, which may only partially cover the aperture, may reduce radiative and convective heat loss as well as particle losses through the aperture.

Table 12. Comparison of solar thermal receiver technologies.

Metric	Solar Thermal Receiver Technology					Ref.
	Falling Particle Receiver	Steam Receiver	Molten Nitrate Salt Receiver	Liquid Sodium Receiver	Volumetric Air Receiver	
Direct energy storage (> 6 hours)?	Yes	No	Yes	No	No	
Maximum irradiance (kW/m ²)	Unlimited (>2,000)	600	600	1,500 – 2,500	900	[10, 51]
Maximum temperature (°C)	>1000 °C up to melting point of particles (2000 °C)	650 °C	<600 °C	800 °C	800 – 900 °C	[10, 51]
Thermal efficiency (%)	80 – 90%	80 – 90%	80 - 90%	90 - 96%	50 – 80%	[1, 3, 52, 53]
Cost (\$/kW _t)	125	~140 – 200	~140 – 200	140 - 200	no data	[49, 54]
Restrictions/ limitations	N/A	High pressure steam requires thicker tubing and more expensive materials	Salt freezes at 200 °C; requires trace heating	Sodium reacts violently with water and spontaneously ignites in air above 115 °C	N/A	
Technology Readiness Level (TRL)	6 Engineering/pilot-scale, prototypical system validation in relevant environment	9 Actual system operated over the full range of expected conditions	9 Actual system operated over the full range of expected conditions	8 Actual system completed and qualified through test and demonstration	8 Actual system completed and qualified through test and demonstration	

Table 13. Comparison of alternative energy-storage systems.

Metric	Energy Storage Technology						Ref.
	Solid Particles	Molten Salt	Batteries	Pumped Hydro	Compressed Air	Flywheels	
Levelized Cost ¹ (\$/MWh _e)	12 - 13	13 - 17	100 – 1,000	150 - 220	120 – 210	350 - 400	[49, 54-56]
Round-trip efficiency ²	>98%	>98%	60 – 90%	65 – 80%	40 – 70%	80 – 90%	[57-60]
Cycle life	>10,000	>10,000	1000 – 5000	>10,000	>10,000	>10,000	[58]
Toxicity/ environmental impacts	N/A	Reactive with piping materials	Heavy metals pose environmental and health concerns	Water evaporation/ consumption	N/A	N/A	
Restrictions/ limitations	Particle/fluid heat transfer can be challenging	< 600 °C (decomposes above ~600 °C)	Very expensive for utility-scale storage	Large amounts of water required	Unique geography required	Only provides seconds to minutes of storage	
Technology Readiness Level (TRL)	6 Engineering/pilot- scale, prototypical system validation in relevant environment	9 Actual system operated over the full range of expected conditions	9 Actual system operated over the full range of expected conditions	9 Actual system operated over the full range of expected conditions	9 Actual system operated over the full range of expected conditions	9 Actual system operated over the full range of expected conditions	

¹ For solid particles and molten salt, we assume a 30 – 35% thermal-to-electric conversion efficiency and 10,000 lifetime cycles for the thermal-to-electric storage and conversion systems; the cost includes the storage media (bulk ceramic particles and sodium/potassium nitrate salts ~\$1/kg with $\Delta T = 400$ °C and 9 hours of storage), tanks, pumps/piping/valves, other parts and contingency, and the power block at \$1000/kW_e with 19 operating hours per daily cycle (including 9 hrs of storage) and 90% availability. For batteries, cost is based on sodium-sulfur, vanadium-redox, zinc-bromine, lead-acid, and lithium-ion batteries capable of providing large-scale electricity.

² Roundtrip efficiency defined as ratio of energy in to energy retrieved from storage

- Reducing particle loss from attrition and wind (currently estimated at ~0.06% of the particle mass flow) by using higher-efficiency (low friction) particle lifts and aperture coverings (e.g., segmented quartz tubes) or multi-stage particle collection and release
 - Particles were observed to be ejected from the aperture due to wind, especially from the south, which created recirculation and a low pressure zone in front of the north-facing aperture that appeared to “suck” particles out of the aperture. The particle level in the collection hopper was periodically leveled and measured, and the mass of particles lost was estimated. Based on the hours of testing, we estimated that we lost ~9 kg/hour or 0.0025 kg/s of particles during testing. Based on an average particle mass flow of ~4 kg/s during the tests, the particle loss was about 0.06% of the mass flow. A particle size distribution analysis from SEM images revealed that about 38% of the total loss was due to attrition (abrasion and wear). The relative particle loss is expected to be less with larger systems due to the increased volume-to-area ratio of the cavity receiver. Additional particles can be added to replenish the inventory, but this will increase costs.
- Enabling variable particle mass flow control and measurement to account for varying DNI and cloud conditions
 - Current test results showed that particle mass flow decreased with increasing temperature due to changes in discharge-plate slot aperture and/or particle/wall friction coefficients. Being able to control and measure the particle mass flow in situ and in real time would be critical to enabling the particles to reach a desired temperature with varying DNI and operating conditions.

Tech to Market

During this project, we have initiated a number of activities to move this technology closer toward commercialization. We collaborated with Abengoa Solar and received a separate contract to model and design a similar 1 MW_t falling particle receiver test facility for their Solucar Platform (which houses PS10 and PS20) near Seville in Spain. We performed modeling and hosted their visits to observe our on-sun testing. In addition, we partnered with the Abengoa Solar Lakewood, CO, office and received an APOLLO award to develop high-temperature falling particle receivers for combined air Brayton cycles. Unfortunately, due to financial problems, Abengoa dissolved the U.S. research, and plans to develop the particle receiver facility in Spain have been put on hold.

We have provided input and consultation to another ELEMENTS project that aims to utilize reduction and oxidation in particles to increase the thermal heating capacity of the particles for air Brayton cycles. Experience from this project has been very valuable for the ELEMENTS thermochemical storage project.

We have also been using our experience and findings from the current project to develop proposals, concepts, and designs for solarized sCO₂ Brayton cycles. This has

led to some technoeconomic studies [61] and some conceptual designs that we plan to use for DOE's upcoming Systems Integration FOA.

Finally, we have designed a marketing brochure that highlights the key attributes of the falling particle receiver relative to other solar thermal receiver technologies. It contains a summary of the key components (particle receiver, storage, heat exchanger, and conveyance) and their performance specifications.

Conclusions

High-temperature falling particle receivers are being pursued to enable higher efficiency, next-generation power cycles operating at $>700\text{ }^{\circ}\text{C}$ for concentrating solar power (CSP). This project developed the world's first continuously operating falling particle receiver (Figure 28) that achieved bulk particle temperatures over $700\text{ }^{\circ}\text{C}$ with free-falling particle mass flow rates up to $\sim 5 - 6\text{ kg/s}$. At lower particle mass flow rates of $\sim 1 - 2\text{ kg/s}$, peak particle temperatures over $900\text{ }^{\circ}\text{C}$ were achieved in the presence of flow obstructions that reduced the particle velocity. Major components that were studied include the particle receiver system, particle optical properties and durability, thermal storage, particle heat exchanger, and particle conveyance.



Figure 28. Images of 1 MW_t particle-receiver system tested at Sandia National Laboratories.

Particle receiver system.

The falling particle receiver is a simple system that directly heats ceramic particles using concentrated sunlight. The 1 MW_t receiver system consists of a 2 m x 2 m x 2 m cubical cavity receiver (through which particles fall) with a 1 m² aperture, a collection hopper, a particle lift to carry the particles back to the top of the receiver, and a top hopper that holds and releases particles into the receiver [1]. Aside from the particle lift, the entire process is based on gravity-driven flow of the particles through each component, reducing parasitic power consumption. Two different receiver designs were tested: free-fall and obstructed flow. The free-fall design is the simplest to implement, but particles can accelerate rapidly, reducing the residence time in the concentrated beam of sunlight and dispersing the particles. Porous obstructions using a staggered array of mesh structures were also designed and tested to slow the particles and increase the residence time. Challenges associated with the mesh include wear and

deterioration at high irradiances with particle abrasion. However, the mesh structures were effective at reducing the particle velocity by an order of magnitude and slowing the terminal velocities to ~ 0.5 m/s, which provided additional particle flow stability and opacity relative to free-fall. On-sun testing of the free-fall particle receiver design showed that the particle temperatures increased by 50 to 200 °C per meter of illuminated drop length for mass flow rates ranging from 1 – 7 kg/s per meter of particle-curtain width and for average irradiances up to ~ 700 kW/m². Higher temperatures were achieved at the lower particle mass flow rates due to less shading. The obstructed flow design yielded particle temperature increases over 300 °C per meter of illuminated drop length for mass flow rates of 1 – 3 kg/s per meter of curtain width for irradiances up to $\sim 1,000$ kW/m². Peak particle temperatures greater than 900 °C were achieved with bulk particle outlet temperatures reaching nearly 800 °C. The thermal efficiencies of both designs reached 70 – 80% at higher irradiances and mass flow rates. At larger scales and higher irradiances, thermal efficiencies approaching 90% are expected based on modeling results. Test results were used to validate computational models of the falling particle receiver performance for different mass flow rates and solar irradiances.

Particles

Studies were performed to identify the ideal size and composition of particles that would be efficiently heated (highly absorptive in the solar spectrum), durable, and affordable. A number of commercially available ceramic particles composed of alumina, silica, and other oxides were tested to evaluate their optical properties and durability. These particles are abundantly available and are used commercially as proppants in the oil and gas industry for hydraulic fracturing. Spherical sintered-bauxite particles were found to be the best candidate material for our application because of its high solar absorptance (>0.9) and resistance to abrasion and sintering at high temperatures and pressures [4, 5]. Testing revealed that the solar weighted absorptance of several proppants maintained $>90\%$ solar weighted absorptance after 500 hours of heating. After nearly 200 hours of on-sun testing, measure particle solar absorptance was essentially the same as unused particles. Formation of iron oxide (hematite) on the particle surface that may change the color of the particles appeared to wear away during testing. Particle loss through attrition and wind was found to be $\sim 0.06\%$ of the average particle mass flow rate. Of the total loss, approximately 38% was due to abrasion (especially from the Olds elevator) and 62% was from loss through the aperture.

Thermal storage

The particle collection hopper used in the prototype system consists of a stainless-steel liner with layers of insulation on the outside. For larger-scale systems operating at potentially higher temperature ($\sim 1,000^\circ\text{C}$), studies were performed to evaluate storage systems comprised of insulating firebrick, insulating concrete, and reinforced concrete [6]. This latter design was modeled and tested at a small scale, and results showed that the heat loss in these systems were less than 5% per day, which corresponded to $\sim 1\%$ per day for larger-scale systems, and cost less than $\$15/\text{kW}_t$.

Particle/working-fluid heat exchanger

Moving packed-bed heat exchangers implementing shell-and-tube and finned shell-and-tube designs were investigated as part of this project to heat a working fluid up to ~ 700 °C. Tests showed that the particle-side heat transfer coefficient was limiting, but could achieve ~ 100 W/m²-K with proper design and spacing of the tubes and fins [7]. Fluidized-bed designs were also characterized from the literature, and higher particle heat transfer coefficients (up to ~ 600 W/m²-K) but with higher parasitic power consumption and heat loss associated with the particle fluidization.

Particle lift

The particle lift used in the prototype system is a stainless-steel Olds elevator that can operate at just over 800 °C. A cylindrical casing rotates about a stationary screw to lift particles up ~ 8 m at a variable controlled rate of up to ~ 10 kg/s. Because the particles are lifted by friction between the particles and the rotating casing, the lift efficiency is low ($\sim 5\%$). For larger-scale systems, an insulated skip hoist system was designed that can achieve $\sim 80\%$ lift efficiency with a parasitic power consumption less than 1% of the rated electrical output of the CSP plant.

Path forward

In order to move forward with larger-scale particle receiver systems (e.g., ≥ 10 MW_e), the additional tests and studies in the following areas should be pursued based on the findings of this project: integration with a particle-to-working-fluid heat exchanger, increased receiver thermal efficiency through scale-up and consideration of alternative geometries and configurations, reduction of particle attrition through higher-efficiency (low-friction) particle lifts, reduction of particle loss through the aperture by consideration of alternative geometries and flow configurations; demonstration of variable particle mass flow control and measurement to account for varying DNI and cloud conditions, and integration and demonstration of a particle-storage and cold-particle-lift unit. Continued collaborations with commercial CSP developers and vendors will also be pursued through on-going and future funding opportunities.

References:

- [1] Ho, C.K., J.M. Christian, J. Yellowhair, K. Armijo, and S. Jeter, 2016, *Performance Evaluation of a High-Temperature Falling Particle Receiver*, in *ASME Power & Energy Conference*, Charlotte, NC, June 26-30, 2016.
- [2] Ho, C.K., J.M. Christian, J. Yellowhair, N. Siegel, S. Jeter, M. Golob, S.I. Abdel-Khalik, C. Nguyen, and H. Al-Ansary, 2015, *On Sun Testing of an Advanced Falling Particle Receiver System*, in *SolarPACES 2015*, Cape Town, South Africa, October 13 - 16, 2015.
- [3] Christian, J.M. and C.K. Ho, 2013, *Alternative Designs of a High Efficiency, North-Facing, Solid Particle Receiver*, in *SolarPACES 2013*, Las Vegas, NV, September 17 - 20, 2013.
- [4] Siegel, N.P., M.D. Gross, and R. Coury, 2015, The Development of Direct Absorption and Storage Media for Falling Particle Solar Central Receivers, *ASME J. Solar Energy Eng.*, **137**(4), p. 041003-041003-7.
- [5] Knott, R., D.L. Sadowski, S.M. Jeter, S.I. Abdel-Khalik, H.A. Al-Ansary, and A. El-Leathy, 2014, *High Temperature Durability of Solid Particles for Use in Particle Heating Concentrator Solar Power Systems*, in *Proceedings of the ASME 2014 8th International Conference on Energy Sustainability*, ES-FuelCell2014-6586, Boston, MA, June 29 - July 2, 2014.
- [6] El-Leathy A. et al., 2013, *Experimental Study of Heat Loss from a Thermal Energy Storage System for Use with a High-Temperature Falling Particle Receiver System*, in *SolarPACES 2013*, Las Vegas, NV, September 17 - 20, 2013.
- [7] Golob et al., 2013, *Serpentine Particle-Flow Heat Exchanger with Working Fluid, for Solar Thermal Power Generation*, in *SolarPACES 2013*, Las Vegas, NV, September 17 - 20, 2013.
- [8] Kolb, G.J., R.B. Diver, and N. Siegel, 2007, Central-station solar hydrogen power plant, *Journal of Solar Energy Engineering-Transactions of the ASME*, **129**(2), p. 179-183.
- [9] Evans, G., W. Houf, R. Greif, and C. Crowe, 1987, Gas-Particle Flow within a High-Temperature Solar Cavity Receiver Including Radiation Heat-Transfer, *Journal of Solar Energy Engineering-Transactions of the ASME*, **109**(2), p. 134-142.
- [10] Falcone, P.K., J.E. Noring, and J.M. Hruby, 1985, Assessment of a Solid Particle Receiver for a High Temperature Solar Central Receiver System, SAND85-8208, Sandia National Laboratories, Livermore, CA.
- [11] Hellmann, J.R., M.O. Eatough, P.F. Hlava, and A.R. Mahoney, 1987, Evaluation of Spherical Ceramic Particles for Solar Thermal Transfer Media, Sandia National Laboratories, SAND86-0981, Albuquerque, NM.
- [12] Hellmann, J.R. and V.S. McConnell, 1986, Characterization of Spherical Ceramic Particles for Solar Thermal Transfer Media: A Market Survey, Sandia National Laboratories, SAND86-1873, Albuquerque, NM.
- [13] Hruby, J.M., 1986, A Technical Feasibility Study of a Solid Particle Solar Central Receiver for High Temperature Applications, SAND86-8211, Sandia National Laboratories, Livermore, CA.

- [14] Hruby, J.M. and B.R. Steele, 1986, A Solid Particle Central Receiver for Solar-Energy, *Chemical Engineering Progress*, **82**(2), p. 44-47.
- [15] Hruby, J.M., B.R. Steele, and V.P. Burolla, 1984, Solid Particle Receiver Experiments: Radiant Heat Test, Sandia National Laboratories, SAND84-8251, Albuquerque, NM.
- [16] Meier, A., 1999, A predictive CFD model for a falling particle receiver reactor exposed to concentrated sunlight, *Chemical Engineering Science*, **54**(13-14), p. 2899-2905.
- [17] Röger, M., L. Amsbeck, B. Gobereit, and R. Buck, 2011, *Face-Down Solid Particle Receiver Using Recirculation*, in *Journal of Solar Energy Engineering-Transactions of the ASME*, 133, 3, Aug.
- [18] Siegel, N., G. Kolb, K. Kim, V. Rangaswamy, and S. Moujaes, 2007, Solid particle receiver flow characterization studies, *Proceedings of the Energy Sustainability Conference 2007*, p. 877-883.
- [19] Kim, K., S.F. Moujaes, and G.J. Kolb, 2010, Experimental and simulation study on wind affecting particle flow in a solar receiver, *Solar Energy*, **84**(2), p. 263-270.
- [20] Siegel, N.P., C.K. Ho, S.S. Khalsa, and G.J. Kolb, 2010, Development and Evaluation of a Prototype Solid Particle Receiver: On-Sun Testing and Model Validation, *Journal of Solar Energy Engineering-Transactions of the ASME*, **132**(2).
- [21] Kolb, G.J., United States Patent U.S. Patent# 8,109,265, 12/368,327, Suction-Recirculation Device for Stabilizing Particle Flows Within a Solar Powered Solid Particle Receiver, Sandia National Laboratories, February 7, 2012.
- [22] Chen, Z.Q., Y.T. Chen, and T.D. Tan, 2009, *Numerical Analysis on the Performance of the Solid Solar Particle Receiver with the Influence of Aerowindow*, in *Proceedings of the ASME Fluids Engineering Division Summer Conference - 2008, Vol 1, Pt a and B*, Jacksonville, FL.
- [23] Tan, T.D. and Y.T. Chen, 2009, *Protection of an Aerowindow, One Scheme to Enhance the Cavity Efficiency of a Solid Particle Solar Receiver*, in *HT2009: Proceedings of the ASME Summer Heat Transfer Conference 2009, Vol 2*, San Francisco, CA.
- [24] Tan, T.D. and Y.T. Chen, 2010, Review of study on solid particle solar receivers, *Renewable & Sustainable Energy Reviews*, **14**(1), p. 265-276.
- [25] Tan, T.D., Y.T. Chen, Z.Q. Chen, N. Siegel, and G.J. Kolb, 2009, Wind effect on the performance of solid particle solar receivers with and without the protection of an aerowindow, *Solar Energy*, **83**(10), p. 1815-1827.
- [26] Ho, C.K. and J.M. Christian, 2013, *Evaluation of Air Recirculation for Falling Particle Receivers*, in *Proceedings of ASME 2013 7th International Conference on Energy Sustainability*, ES-FuelCell2013-18236, Minneapolis, MN, July 14 - 19, 2013.
- [27] Ho, C.K., J.M. Christian, A.C. Moya, J. Taylor, D. Ray, and J. Kelton, 2014, *Experimental and Numerical Studies of Air Curtains for Falling Particle Receivers*, in *Proceedings of ASME 2014 8th International Conference on Energy Sustainability*, ES-FuelCell2014-6632, Minneapolis, MN, June 29 - July 2, 2014.
- [28] Ho, C.K., J.M. Christian, D. Romano, J. Yellowhair, and N. Siegel, 2015, *Characterization of Particle Flow in a Free-Falling Solar Particle Receiver*, in

- Proceedings of the ASME 2015 Power and Energy Conversion Conference*, PowerEnergy2015-49421, San Diego, CA, June 28 - July 2, 2015.
- [29] Khayyat, A.W., R.C. Knott, C.L. Nguyen, M.C. Golob, S.I. Abdel-Khalik, S.M. Jeter, and H.A. Al-Ansary, 2015, *Measurement of Particulate Flow in Discrete Structure Particle Heating Receivers*, in *Proceedings of the ASME 2015 Power and Energy Conversion Conference*, San Diego, CA, June 28 - July 2, 2015.
- [30] Lee, T., S. Lim, S. Shin, D.L. Sadowski, S.I. Abdel-Khalik, S.M. Jeter, and H. Al-Ansary, 2015, Numerical simulation of particulate flow in interconnected porous media for central particle-heating receiver applications, *Solar Energy*, **113**, p. 14-24.
- [31] Ho, C.K., S.S. Khalsa, and N.P. Siegel, 2009, *Modeling on-Sun Tests of a Prototype Solid Particle Receiver for Concentrating Solar Power Processes and Storage*, in *ES2009: Proceedings of the ASME 3rd International Conference on Energy Sustainability*, Vol 2, San Francisco, CA.
- [32] Jeter, 2013, Statistical Analysis of Sand Accumulation Experiment, GIT. 2013.
- [33] Roop, J., S. Jeter, S.I. Abdel-Khalik, and C.K. Ho, 2014, *Optical Properties of Select Particulates After High-Temperature Exposure*, in *Proceedings of ASME 2014 8th International Conference on Energy Sustainability*, ES-FuelCell2014-6504, Boston, MA, June 29 - July 2, 2014.
- [34] A. Khayyat, e.a., Year, *Measurement of Particle Flow in Discrete Structure Particle Heating Receivers*, in *ASME 2015 9th International Conference on Energy Sustainability*, San Diego, CA.
- [35] C. Nguyen, e.a., 2014, "Study of Solid Particles as a Thermal Medium," *Energy Procedia*, **49**, p. 637-646.
- [36] Knott, R., *High Temperature Durability of Metals for use in Particle Heating Receiver for Concentrator Power*, 2014.
- [37] J. Roop, e.a., Year, *Computational Analysis of Particulate Storage Bin for High Temperature Thermal Energy Storage*, in *ASME 2014 8th International Conference on Energy Sustainability*, Boston, MA.
- [38] T. Lee, e.a., 2015, Numerical Simulation of Particulate Flow in Interconnected Porous Media for Central Particle-Heating Receiver Applications, *Solar Energy*, **113**, p. 14-24.
- [39] Nguyen, C., Golob, M., Jeter, S., 2015, Uncertainty Analysis Methodology For Particle Heating Receiver Testing, Proceedings, Fifteenth Annual Early Career Technical Conference, Birmingham, AL, November.
- [40] M. Golob, e.a., Year, *Development and Design Prototype 300 KW-Thermal High Temperature Particle Heating Concentrator Solar Power System Utilizing Thermal Energy Storage*, in *ASME 2014 8th International Conference on Energy Sustainability* Boston, MA.
- [41] Golob, e.a., 2015, Solar Simulator Mixed Temperature Test of Wire Mesh Particle Heating Receiver to measure receiver efficiency, Proceedings, Fifteenth Annual Early Career Technical Conference, Birmingham, AL, November.
- [42] Siegel, N., M. Gross, C. Ho, T. Phan, and J. Yuan, 2014, Physical properties of solid particle thermal energy storage media for concentrating solar power applications, *Proceedings of the Solarpaces 2013 International Conference*, **49**(Energy Procedia), p. 1015-1023.

- [43] Knott, R., D.L. Sadowski, S.M. Jeter, S.I. Abdel-Khalik, H.A. Al-Ansary, and A. El-Leathy, 2014, *Sintering of Solid Particulates under Elevated Temperature and Pressure in Large Storage Bins for Thermal Energy Storage*, in *Proceedings of the ASME 2014 8th International Conference on Energy Sustainability*, ES-FuelCell2014-6588, Boston, MA, June 29 - July 2, 2014.
- [44] Sadowski, M.G.a.D., 2013, Serpentine Particle-Flow Heat Exchanger with Working Fluid, for Solar Thermal Power Generation, ASME Early Career Technical Conference, 2013 ASME Early Career Technical Conference, ASME ECTC, Birmingham, AL Nov 2 – 3.
- [45] Repole, R.a.J., S., 2015, *Application of a Sequence of a Design Methodologies to the Problem of Transporting Warm Particles in Particle Heating Receiver Solar Energy Systems*, in *ECTC 2015*, Birmingham, AL,
- [46] K. Repole, e.a., Year, *Preliminary Commercial Design for Transporting Low Temperature Particles for Use in Particle Solar Receivers Using Lifting Skips*, in *Early Career Technical Conference*, Birmingham, AL,
- [47] Repole, K.a.S.J., 2016, Design and Analysis of a High Temperature Particulate Hoist for Proposed Particle Heating Concentrator Solar Power Systems, *Proceedings of the 2016 ASME Power and Energy Conference*, PowerEnergy2016 June 26-30, 2016, Charlotte, North Carolina.
- [48] Bradshaw, R.W. and D.E. Meeker, 1990, High-Temperature Stability of Ternary Nitrate Molten-Salts for Solar Thermal-Energy Systems, *Solar Energy Materials*, **21**(1), p. 51-60.
- [49] Ho, C.K., 2016, A Review of High-Temperature Particle Receivers for Concentrating Solar Power, *Applied Thermal Engineering*, (available online 3 May 2016: <http://dx.doi.org/10.1016/j.applthermaleng.2016.04.103>).
- [50] Amsbeck, L., G. Hellsch, M. Roger, and R. Uhlig, 2009, *Development of a Broadband Antireflection Coated Transparent Silica Window for a Solar-Hybrid Microturbine Systems*, in *Proceedings of SolarPACES 2009*, Berlin, Germany, September 15 - 18, 2009.
- [51] Hoffschmidt, B., F.M. Tellez, A. Valverde, J. Fernandez, and V. Fernandez, 2003, Performance evaluation of the 200-kW(th) HiTRec-II open volumetric air receiver, *Journal of Solar Energy Engineering-Transactions of the Asme*, **125**(1), p. 87-94.
- [52] Ho, C.K. and B.D. Iverson, 2014, Review of high-temperature central receiver designs for concentrating solar power, *Renewable & Sustainable Energy Reviews*, **29**, p. 835-846.
- [53] International, R., 1983, Final Report Sodium Solar Receiver Experiment, SAND82-8192, Sandia National Laboratories. December 1983.
- [54] Kolb, G.J., Ho, C.K., Mancini, T.R., Gary, J.A., 2011, Power Tower Technology Roadmap and Cost Reduction Plan, SAND2011-2419, Sandia National Laboratories, Albuquerque, NM.
- [55] Branz, H.M., W. Regan, K.J. Gerst, J.B. Borak, and E.A. Santori, 2015, Hybrid solar converters for maximum exergy and inexpensive dispatchable electricity, *Energy & Environmental Science*, **8**(11), p. 3083-3091.
- [56] Akhil, A.A., 2015, DOE/EPRI Electricity Storage Handbook in Collaboration with NRECA, Sandia National Laboratories, SAND2015-1002, Albuquerque, NM.

- [57] Djajadiwinata, E., H. Al-Ansary, S. Danish, A. El-Leathy, and Z. Al-Suhaibani, 2014, Modeling of Transient Energy Loss from a Cylindrical-Shaped Solid Particle Thermal Energy Storage Tank for Central Receiver Applications, *Proceedings of the Asme 8th International Conference on Energy Sustainability, 2014, Vol 1*.
- [58] Siegel, N.P., 2012, Thermal energy storage for solar power production, *Wiley Interdisciplinary Reviews-Energy and Environment*, **1**(2), p. 119-131.
- [59] Energy Storage Association. *Energy Storage Technologies*. 2016; Available from: <http://energystorage.org/energy-storage/energy-storage-technologies>.
- [60] EnergyMag. *Round Trip Efficiency*. 2016; Available from: <https://energymag.net/round-trip-efficiency/>.
- [61] Ho, C.K., M. Carlson, P. Garg, and P. Kumar, 2015, *Cost And Performance Tradeoffs Of Alternative Solar-Driven S-Co2 Brayton Cycle Configurations*, in *Proceedings of the ASME 2015 Power and Energy Conversion Conference*, San Diego, June 28 - July 2, 2015.